



# Seawater $\delta^7\text{Li}$ : A direct proxy for global $\text{CO}_2$ consumption by continental silicate weathering?



Christoph Wanner<sup>a,\*</sup>, Eric L. Sonnenthal<sup>a</sup>, Xiao-Ming Liu<sup>b,c</sup>

<sup>a</sup> Earth Sciences Division, Lawrence Berkeley National Laboratory, 1 Cyclotron Road, Berkeley, CA 94720, USA

<sup>b</sup> Geophysical Lab, Carnegie Institute of Washington, DC 20015, USA

<sup>c</sup> Department of Geology, University of Maryland – College Park, College Park, MD 20742, USA

## ARTICLE INFO

### Article history:

Received 11 February 2014

Received in revised form 6 May 2014

Accepted 8 May 2014

Available online 16 May 2014

Editor: Michael E. Böttcher

### Keywords:

Li isotopic fractionation

Seawater  $\delta^7\text{Li}$

Silicate weathering

Reactive transport modeling

$\text{CO}_2$  consumption

## ABSTRACT

The fractionation of stable Li isotopes ( $^6\text{Li}$ ,  $^7\text{Li}$ ) has become a promising proxy for assessing changes related to continental silicate weathering patterns. Recently, the first complete record of Cenozoic seawater Li isotopic composition ( $\delta^7\text{Li}$ ) was reported (Misra and Froelich, 2012, *Science* 335, 818–821) showing a stepwise increase of +9‰ over the last 56 Ma. This increase was attributed to a general change in continental silicate weathering behavior caused by tectonic uplift. In particular, the low global average riverine  $\delta^7\text{Li}$  inferred for the Paleocene–Eocene boundary was explained by congruent silicate weathering of primary silicate minerals, which is inconsistent with the stoichiometry of secondary minerals and the resultant water chemistry.

In this study, we present a novel reactive transport modeling approach that explicitly includes Li isotopic fractionation to assess alternative geochemically-constrained interpretations that do not rely on congruent weathering. Simulations show that riverine  $\delta^7\text{Li}$  is mainly controlled by the subsurface residence time, the corresponding weathering intensity, and the concentration of a river's suspended load. Based on these factors, we suspect that the low  $\delta^7\text{Li}$  observed at the Paleocene–Eocene boundary was inherited from a high weathering intensity with predominant weathering of previously formed secondary mineral phases (e.g., clays, oxides) having low  $\delta^7\text{Li}$  values. Moreover, we conclude that the Cenozoic  $\delta^7\text{Li}$  increase was caused by an increasing amount of primary silicate mineral dissolution inherited from an increasing suspended river load concentration and a decreasing weathering intensity both likely induced by tectonic uplift. In contrast, Cenozoic cooling and corresponding  $p\text{CO}_2$  and precipitation variations do not seem to have a distinct control on the Cenozoic  $\delta^7\text{Li}$  record. Finally, our simulations revealed a close relation between  $\delta^7\text{Li}$  and  $\text{CO}_2$  consumption by silicate weathering implying that the Cenozoic seawater  $\delta^7\text{Li}$  record could be potentially used to quantify such  $\text{CO}_2$  consumption through time. However, more experimental and modeling work is required to quantify the correlation between seawater  $\delta^7\text{Li}$  and global  $\text{CO}_2$  consumption by silicate weathering. Key parameters are the temperature-dependent thermodynamic properties of specific Li-bearing primary and secondary minerals (e.g., crystallographic Li substitution reaction, maximum Li substitution, Li solubility, Li isotopic fractionation factor) as well as the determination of global average subsurface and river discharges through time.

© 2014 Elsevier B.V. All rights reserved.

## 1. Introduction

Continental chemical weathering forms a major  $\text{CO}_2$  sink and is therefore an important input parameter for climate models (e.g., Berner et al., 1983; Francois and Godderis, 1998; Berner and Kothavala, 2001; Godderis et al., 2009; Li and Elderfield, 2013). However, the present and past global  $\text{CO}_2$  consumption by continental silicate weathering has not been precisely quantified (Li and Elderfield, 2013). Climate models simulating the carbon cycle over Earth's history typically calibrate  $\text{CO}_2$  consumption by chemical weathering against the observed seawater  $^{87}\text{Sr}/^{86}\text{Sr}$  ratio. Using  $^{87}\text{Sr}/^{86}\text{Sr}$  is challenging because it reflects

chemical weathering of carbonates, as well as weathering of silicate minerals (Oliver et al., 2003; Godderis et al., 2009). Tracking the individual contribution of continental silicate weathering is, however, crucial because it may demonstrate whether an observed global  $\text{CO}_2$  drawdown is caused by increased tectonic activity, such as the onset of the Himalayan orogeny ca. 30 Ma ago (Raymo and Ruddiman, 1992), or by a decrease in total Earth  $\text{CO}_2$  degassing (Berner et al., 1983). In contrast to Sr, lithium is a trace element that is almost exclusively found in silicate minerals, which makes it a useful tracer for silicate weathering (e.g., Huh et al., 1998, 2001; Kisakürek et al., 2004; Rudnick et al., 2004; Kisakürek et al., 2005; Pogge von Strandmann et al., 2006; Vigier et al., 2009; Millot et al., 2010; Pogge von Strandmann et al., 2010; Liu et al., 2013). In particular, tracking Li isotopic fractionation is promising because the two stable Li isotopes ( $^6\text{Li}$ ,  $^7\text{Li}$ ) fractionate

\* Corresponding author. Tel.: +1 5104958147.

E-mail addresses: [cwanner@lbl.gov](mailto:cwanner@lbl.gov), [christoph.wanner@geo.unibe.ch](mailto:christoph.wanner@geo.unibe.ch) (C. Wanner).

when Li-bearing primary silicate minerals (e.g., micas) are weathered and secondary mineral phases (e.g., clays) are formed (Zhang et al., 1998; Pistiner and Henderson, 2003; Vigier et al., 2008; Wimpenny et al., 2010a).

Hathorne and James (2006) presented the first record of seawater Li isotopic composition ( $\delta^7\text{Li}$ ) over the past 18 Ma using foraminifera as a proxy. Misra and Froelich (2012) extended the record to 68 Ma showing a +9‰ increase over the last ca. 56 Ma. Unlike the steady  $^{87}\text{Sr}/^{86}\text{Sr}$  increase,  $\delta^7\text{Li}$  increased stepwise, which was attributed to specific tectonic events (e.g., Himalayan orogeny) (Misra and Froelich, 2012). Specifically, the latter authors argued that tectonic uplift shifted the global silicate weathering pattern from a congruent, transport-limited regime to an incongruent, weathering-limited regime. However, the latter interpretation cannot be fully justified from a geochemical perspective, because secondary minerals typically observed under a transport-limited weathering regime (e.g., Fe- and Al-oxides) are inconsistent with congruent silicate weathering.

Among the earth sciences, reactive transport modeling has become a powerful tool for a predictive understanding of many subsurface systems (Steeffel et al., 2005). To the best of our knowledge, it has not yet been used for a quantitative understanding of Li isotopic fractionation processes. Instead, field-derived Li isotopic data were usually explained by using closed system Rayleigh distillation models (Kisakürek et al., 2004; Rudnick et al., 2004; Yoon, 2010; Tipper et al., 2012). Such models greatly simplify Li isotope fractionation processes because they only consider fractionation effects associated with the precipitation of Li-bearing minerals from an aqueous solution having a specific initial Li concentration. In contrast, they neglect that aqueous Li concentrations, and thus corresponding Li isotope fractionation effects, are also controlled by the simultaneous dissolution of Li-bearing primary minerals. Recently, Bouchez et al. (2013) presented a box-type mass balance and flux model that considers both dissolution of Li-bearing primary minerals and the precipitation of Li-bearing secondary minerals. Similar to Rayleigh-type models, the Bouchez et al. (2013) model does not take into account mineralogical, kinetic and thermodynamic properties of mineral phases involved in Li isotope fractionation processes (e.g., mineral stoichiometry, dissolution and precipitation rates, mineral solubilities).

In this paper we present a reactive transport modeling approach explicitly including the fractionation of Li isotopes to quantitatively test alternative interpretations for the Cenozoic seawater  $\delta^7\text{Li}$  record that do not rely on congruent silicate weathering. By doing so, we show that global average riverine and seawater  $\delta^7\text{Li}$  values are mainly controlled by the cumulative extent of water–rock interaction taking place along a flow path and are thus closely related to the corresponding  $\text{CO}_2$  consumption.

## 2. Global Li isotopic fractionation model

### 2.1. The Misra and Froelich (2012) model

Using a mass balance approach Misra and Froelich (2012) argued that the change in seawater  $\delta^7\text{Li}$  was solely attributed to a change in riverine  $\delta^7\text{Li}$ . The conclusion that changing seawater  $\delta^7\text{Li}$  values are mainly caused by a changing fate of continental Li seems reasonable as there is evidence that the seawater hydrothermal fluid input and oceanic Li isotopic fractionation processes remained roughly constant during the Cenozoic (Rowley, 2002; Müller et al., 2008). However, the rate of past oceanic crust production is still under debate. For example, various GEOCARB models (e.g., Berner, 1994; Berner and Kothavala, 2001) consider a variable hydrothermal fluid input. Moreover, the low seawater  $\delta^7\text{Li}$  values observed at the Paleocene–Eocene boundary (Misra and Froelich, 2012) could be inherited from a lower global average riverine  $\delta^7\text{Li}$  value (at constant riverine Li flux), from a lower dissolved riverine Li flux (at a constant  $\delta^7\text{Li}$  value), or from a combination of both. In fact, it is rather unlikely that processes causing a shift of the global average

riverine Li isotopic composition do not vary the global average riverine Li flux and [Li].

It is well accepted that Li isotopic fractionation is mainly associated with secondary mineral precipitation (Kisakürek et al., 2005; Pogge von Strandmann et al., 2006; Vigier et al., 2009; Millot et al., 2010; Pogge von Strandmann et al., 2010). By contrast, Li isotopes stoichiometrically dissolve from primary silicate minerals (Pistiner and Henderson, 2003; Huh et al., 2004). Riverine  $\delta^7\text{Li}$  is thus controlled by the ratio of Li released by primary silicate mineral dissolution to Li removed by secondary mineral precipitation and by Li isotopic fractionation associated with precipitation. Consequently, host rock mineralogy does not show a distinct control on riverine  $\delta^7\text{Li}$  (Kisakürek et al., 2005; Millot et al., 2010). Changing global average riverine  $\delta^7\text{Li}$  values thus reflect a changing silicate weathering pattern only.

For the Paleocene–Eocene boundary (~56 Ma ago) a global average riverine  $\delta^7\text{Li}$  value of +3‰ was inferred (Misra and Froelich, 2012), being ca. 20‰ lower than the average  $\delta^7\text{Li}$  value of modern rivers. Misra and Froelich (2012) concluded that this light value was inherited from congruent weathering of primary silicate minerals having a  $\delta^7\text{Li}$  value in the same order of magnitude, whereas the current value is inherited from incongruent silicate weathering including secondary mineral precipitation (e.g., clays, oxides, and hydroxides) and accompanying Li isotopic fractionation. Whereas average continental bulk rock  $\delta^7\text{Li}$  values close to +3‰ are justified by the studies of Teng et al. (2004, 2008, 2009) reporting  $\delta^7\text{Li}$  values for the average ( $\delta^7\text{Li} = +2.0 \pm 2.3\%$ ), upper ( $\delta^7\text{Li} = 0 \pm 2\%$ ) and lower continental crust ( $\delta^7\text{Li} = +1.6 \pm 8.9\%$ ), congruent silicate weathering seems rather questionable. Specifically, Misra and Froelich (2012) argued that the global weathering regime at the Paleocene–Eocene boundary was similar to the current low-relief, peneplained type and transport-limited weathering pattern inferred for the Guayana Shield (Edmond et al., 1995). The Guayana Shield is located at the border of Venezuela, Colombia and Brazil and one of the so far lowest riverine  $\delta^7\text{Li}$  values was measured for a sample collected from this area (+6.6‰, Huh et al., 1998). Edmond et al. (1995) indeed characterized the weathering regime of the Guayana Shield as being weathering-intense and transport-limited but they explicitly stated that primary silicate minerals are incongruently dissolved. In fact, only incongruent silicate mineral dissolution can explain the formation of thick saprolites with an accumulation of quartz, clays, Fe- and Al-oxides typically observed at locations experiencing a high weathering intensity (White et al., 2001; Kisakürek et al., 2004; Rudnick et al., 2004; Liu et al., 2013). Incongruent silicate weathering is also consistent with the low Al solubility at near neutral pH values, typical of these systems.

Furthermore, it is questionable if the average riverine  $\delta^7\text{Li}$  value at the Paleocene–Eocene boundary was as low as +3‰. If this is true, similar riverine  $\delta^7\text{Li}$  values should be found somewhere on Earth today reflecting weathering conditions for an isolated location that are similar to the global weathering pattern observed in the past (Hathorne and James, 2006). In fact, the compilation of available current riverine  $\delta^7\text{Li}$  values showed that the minimum values were larger, on the order of 6‰ (Misra and Froelich, 2012). Values close to +6‰, however, have so far only been published for two specific samples and only one of them originated from a weathering intense location (Guyana Shield, Huh et al., 1998). The other sample was collected from a Siberian river (Yana) where the weathering intensity is lower (Huh et al., 1998). Nevertheless, it is notable that +6‰ is in the same order of magnitude as the asymptotic riverine  $\delta^7\text{Li}$  value Misra and Froelich (2012) obtained for the Paleocene–Eocene ocean by performing a sensitivity analysis on their mass balance calculations. Based on this analysis, the lack of present river  $\delta^7\text{Li}$  values less than +6‰, and a recent refinement of the Li cycle at the Paleocene–Eocene boundary ( $\delta^7\text{Li}_{\text{riverine}} = +12\%$ , Li and West, 2014), we propose that the Paleocene–Eocene riverine  $\delta^7\text{Li}$  was likely around +6‰ or larger. Inferring a global average riverine  $\delta^7\text{Li}$  that is higher than the value of the upper continental crust ( $\delta^7\text{Li} = 0.0 \pm 2\%$ , Teng et al., 2004) implies that Li isotopic fractionation between bulk

crustal rocks and global rivers was taking place. Moreover, it rules out congruent weathering as being responsible for the minimum seawater  $\delta^7\text{Li}$  observed at the Paleocene–Eocene boundary.

## 2.2. Alternative hypotheses explaining the Cenozoic seawater $\delta^7\text{Li}$ value record

Following the arguments of Misra and Froelich (2012), we assume that increasing Cenozoic seawater  $\delta^7\text{Li}$  values are mainly attributed to a change in riverine  $\delta^7\text{Li}$ . We do, however, not *a priori* assume that the riverine Li flux and the hydrothermal seawater Li input remained constant. Nevertheless, we focus on changing riverine  $\delta^7\text{Li}$  values rather than on the possible effects of changing Li isotopic fractionation processes in the ocean (i.e., reverse weathering) and of a variable seawater hydrothermal Li input. Also, we assume that the composition of the continental crust exposed to chemical weathering remained roughly constant since the Paleocene–Eocene boundary, thus neglecting the potential effects of time-varying lithology on global average riverine and seawater  $\delta^7\text{Li}$  values. Similar to Misra and Froelich (2012), we speculate that the Cenozoic seawater  $\delta^7\text{Li}$  value increase is most likely inherited from a changing continental silicate weathering pattern induced by an increasing global relief owing to major global orogenies (e.g., Himalayan, Andean orogeny) and by the cooling trend observed since the humid Paleocene–Eocene thermal maximum (PETM) (Miller et al., 1987;

Clementz and Sewall, 2011). An increasing relief (Fig. 1) and cooler temperatures have the following first order effects on chemical silicate weathering, which have potentially caused the observed  $\delta^7\text{Li}$  shift:

- 1) An increasing relief shifts the hydraulic gradient to higher values, increasing flow velocities and shortening residence times along a specific subsurface flow path (Fig. 1). Cooler temperatures decrease the dissolution rates of primary silicate minerals (Lasaga, 1984). Hence, increasing relief and cooler temperatures limit water–rock interaction along specific flow paths.
- 2) For a low relief, such as inferred for the Paleocene–Eocene boundary (Misra and Froelich, 2012), the hydraulic gradient is low and the average subsurface residence time is high. Long residence times under hot and humid climatic conditions (Miller et al., 1987; Clementz and Sewall, 2011) cause a high degree of water rock–interaction with plenty of newly formed secondary mineral phases, which is usually described as a weathering–intensive or transport–limited weathering pattern (Misra and Froelich, 2012). We thus assume that at the Paleocene–Eocene boundary, the global average saprolite thickness (composed of mostly quartz, clays, Fe- and Al-oxides) was higher than it is today (Fig. 1). Following this argument, and taking into account an increasing global relief as well as decreasing temperatures, the degree of exposure of the silicate bedrock to chemical weathering must have increased over the last 56 Ma, which is equivalent to proposing a decreasing weathering intensity. It should be noted that our use of “weathering intensity” throughout this paper strictly refers to the chemical index of alteration (CIA), which is the commonly used proxy for expressing the chemical weathering intensity of a particular rock or soil sample (Nesbitt and Young, 1982). This definition is particularly useful because it takes into account the ratio between immobile (e.g., Al) and mobile (e.g., Na, Ca, K) elements, on which the amount of newly formed clays, oxides and hydroxides has a first order control. Alternatively, riverine aqueous species concentrations (e.g., [Si], normalized [Si]) have been proposed to operate as weathering intensity proxies (Kisakürek et al., 2005; Pogge von Strandmann et al., 2006). The drawback of using riverine aqueous species concentrations is that, once chemical equilibrium is reached, their concentrations become discharge independent (Maher, 2011), whereas chemical silicate weathering fluxes and corresponding weathering rates are linearly increasing with increasing discharge (Gaillardet et al., 1999; Maher, 2011). The strong dependence on discharge also implies that chemical silicate weathering rates do not necessarily correspond to weathering intensity. For instance, a relatively low chemical weathering rate was calculated for the weathering intense Guyana Shield (Gaillardet et al., 1999).
- 3) Owing to the higher hydraulic gradient, an increasing global relief shifts the physical erosion rate (i.e., denudation rate) to higher values (Bouchez et al., 2013). A higher denudation rate leads to an increase of the suspended river load concentration, as long as the suspended load is not deposited in lowland areas (Milliman and Meade, 1983; Gaillardet et al., 1999). Consequently, we speculate that the global average suspended river load concentration increased over the last 56 Ma such as already argued by Misra and Froelich (2012).

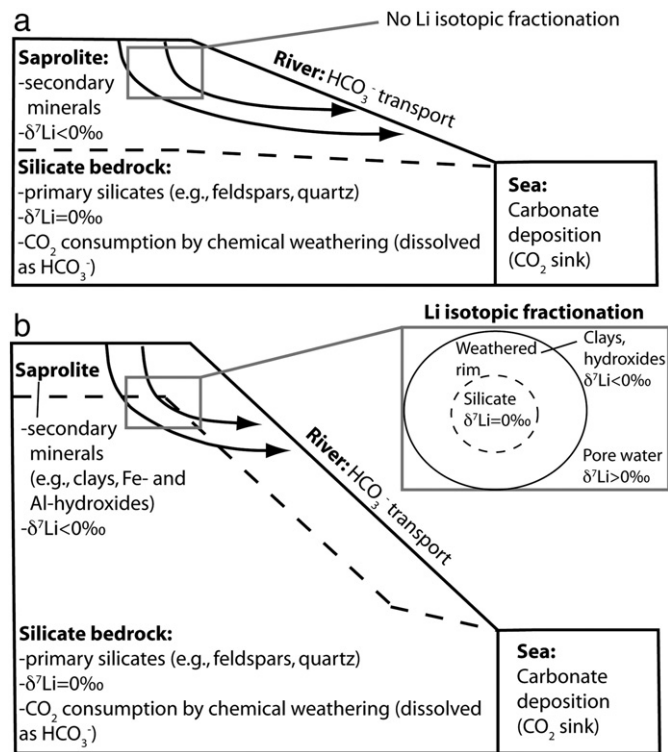


**Fig. 1.** Proposed weathering and Li isotopic fractionation model for the Paleocene–Eocene boundary (a) and for today (b) in terms of idealized crustal cross sections along a major river system. Black arrows show typical flow paths for meteoric water infiltrating into the subsurface and being transported in groundwater systems before exfiltrating into a major river system. Increasing Cenozoic seawater  $\delta^7\text{Li}$  values (Misra and Froelich, 2012) are explained by an increasing availability of bedrock (primary) silicates for chemical weathering (i.e., decreasing weathering intensity) as the global relief increases and the average saprolite thickness becomes smaller. For the current weathering pattern, chemical weathering of primary silicates and subsequent precipitation of secondary minerals (clays, Fe- and Al-hydroxides) fractionate Li isotopes by accumulating  $^7\text{Li}$  in the groundwater and  $^6\text{Li}$  in the precipitating mineral phases. If only secondary silicate minerals are exposed to chemical weathering such as inferred for the Paleocene–Eocene boundary (a) no significant Li isotopic fractionation occurs. An increasing relief also yields decreasing subsurface residence times as well as increasing suspended river load concentrations, both potentially affecting riverine  $\delta^7\text{Li}$  in addition to the decreasing weathering intensity.

## 3. Methods

A series of thermodynamically- and kinetically-controlled reactive transport model simulations using TOUGHREACT V2 (Xu et al., 2011) was performed to assess the effect of the identified changing weathering parameters on Cenozoic global average riverine and seawater  $\delta^7\text{Li}$  (i.e., decreasing subsurface residence time, cooling trend, decreasing weathering intensity, increasing suspended river load concentration). TOUGHREACT has been used to evaluate isotopic fractionation coupled to water–rock interaction and hydrological processes in a variety of

subsurface environments and laboratory experiments (e.g., [Sonnenthal et al., 1998](#); [Singleton et al., 2005](#); [Wanner and Sonnenthal, 2013](#)).

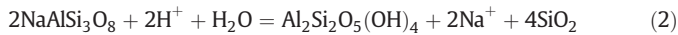
### 3.1. Model setup

Two different types of simulations were carried out to model silicate weathering and associated Li isotopic fractionation (i) in the subsurface and (ii) within rivers ([Fig. 2](#)).

#### 3.1.1. Subsurface simulations

Reactive transport of infiltrating meteoric water along a typical subsurface flow path (e.g., arrows in [Fig. 1](#)) was simulated for a fully water-saturated, 200 m long porous media with an assumed porosity of 10%. The unsaturated zone was neglected because our focus was on assessing the sensitivity (i.e., trends) of dissolved  $\delta^7\text{Li}$  values as a function of residence time, climate, and weathering intensity rather than on simulating detailed flow features of infiltration through the unsaturated zone and recharge to aquifers and rivers. Subsurface simulations were run for an average linear flow velocity of 1 m/d to simulate a system dominated by advection. The 200 m long model domain ([Fig. 2](#)) was divided into 200 cubic grid blocks of  $1 \times 1 \times 1$  m each to numerically solve the governing differential equations using TOUGHREACT's integral finite differences approach ([Xu et al., 2011](#)).

Pure water in equilibrium with atmospheric  $\text{CO}_2$  was specified as initial and boundary fluid compositions. In doing so, atmospheric  $\text{CO}_2$  is partially dissolved and provides  $\text{H}^+$  necessary for silicate weathering reactions such as illustrated for the weathering of albite to kaolinite:



The  $\text{CO}_2$  partial pressure  $p\text{CO}_2$  was fixed during the course of the simulations to approximate the buffering caused by an almost unlimited  $\text{CO}_2$  source from the atmosphere. This specification allows tracking the amount of  $\text{CO}_2$  consumed by silicate weathering reactions assuming that the reaction product  $\text{HCO}_3^-$  exiting the model domain is further transported to the sea, where it precipitates as carbonates ([Godderis et al., 2009](#)) ([Fig. 1](#)).

A granitic mineral assemblage (quartz, potassium-feldspar, plagioclase, biotite) was assigned to the solid part of the porous media to simulate typical continental silicate weathering processes. Subsequently, the model was divided into a “fresh granite” domain and a domain

that experienced previous weathering (e.g., “altered granite”) ([Fig. 2](#)), thus corresponding to the saprolite zone of our conceptual model ([Fig. 1](#)). By varying the volume ratio between the “fresh granite” and “altered granite” domain the effect of the proposed increasing exposure of the silicate bedrock to chemical weathering on  $\delta^7\text{Li}$  was assessed. By running the model for a variable “fresh granite” contribution (i.e., varying volume ratios) we simulated the effect of a varying chemical weathering intensity (i.e., varying saprolite thicknesses) on  $\delta^7\text{Li}$  because a large “fresh granite” or large “altered granite” contribution corresponds to a low or high weathering intensity, respectively. Accordingly, we also assess earlier findings reporting that the chemical silicate weathering intensity forms a first order control on aqueous  $\delta^7\text{Li}$  ([Huh et al., 2001](#); [Kisakürek et al., 2005](#); [Pogge von Strandmann et al., 2006](#)).

A mineralogical composition typical for the Sierra Nevada Batholith ([Economos et al., 2010](#)) was defined for the “fresh granite” domain ([Table 1](#)). The initial mineralogical definition included a bulk Li concentration of 24 ppm ([Economos et al., 2010](#)), which is similar to the average upper-crustal Li concentration of  $35 \pm 11$  ppm ([Teng et al., 2004](#)). Owing to their similar ionic radii,  $\text{Li}^+$  substitutes easily for  $\text{Mg}^{2+}$  into the structural octahedral sites of silicate minerals ([Vigier et al., 2008](#)). Furthermore, Li tends to accumulate in biotite ([Kretz et al., 1989](#)). Accordingly, Li was introduced into the model by specifying Li-bearing biotite using a  $\text{Mg}^{2+} - \text{Li}^+ / \text{K}^+$  exchange ([Table 2](#)). Because in granitic environments, silicate mineral phases are predominantly weathered to kaolinite ([White, 2002](#); [Rudnick et al., 2004](#); [Maher et al., 2009](#)), and because goethite is the most widespread form of secondary iron oxides ([Tardy and Nahon, 1985](#)) Li-bearing kaolinite, and Li-bearing goethite were allowed to precipitate. By neglecting secondary Ca- and Mg-bearing minerals we do not fully investigate the fate of these two elements during silicate weathering. Our conceptual model ([Fig. 1](#)), however, assumes that riverine [Ca] and [Mg] are affected by carbonate weathering to ensure that carbonate precipitation and subsequent  $\text{CO}_2$  consumption are occurring in the ocean, eventually.

TOUGHREACT V2 ([Xu et al., 2011](#)) computes mineral dissolution and precipitation reactions as kinetic reactions based on transition state theory (TST) ([Lasaga, 1984](#))

$$r = A \cdot k \cdot \left(1 - \left(\frac{Q}{K}\right)^m\right)^n \quad (3)$$

where A refers to the mineral reactive surface area ( $\text{m}^2_{\text{mineral}}/\text{kg}_{\text{H}_2\text{O}}$ ), k is the reaction rate constant ( $\text{mol}/\text{m}^2/\text{s}$ ), Q refers to the ion activity product of a mineral dissolution/precipitation reaction ([Table 2](#)) and K is the corresponding equilibrium constant. Exponents m and n are

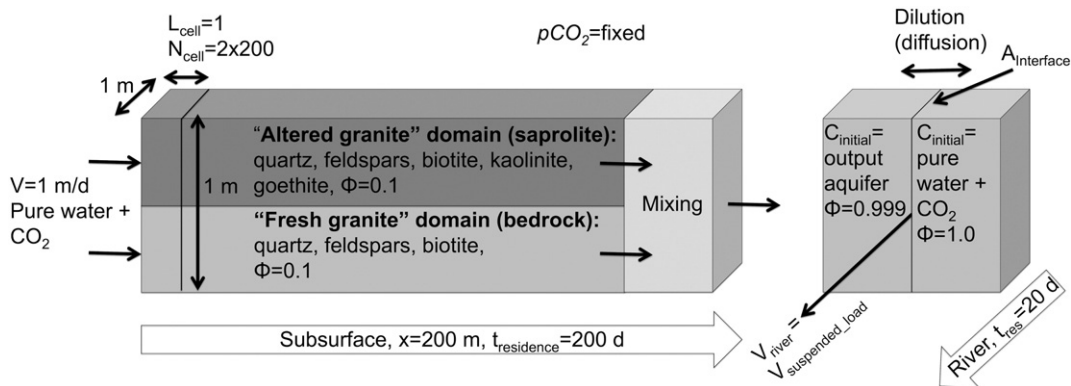


**Fig. 2.** Model setup for simulating reactive transport in the subsurface and within rivers. Subsurface simulations were run for meteoric water infiltrated and transported along a 200 m long flow path eventually exfiltrating into a river system (e.g., arrows in [Fig. 1](#)). They were run for various fresh-to-altered granite volume fractions to simulate the effects of a varying silicate weathering intensity on  $\delta^7\text{Li}$ . Fluids flowing along the two model domains were fully mixed in the downstream model boundary (“mixing”) to track the integrated Li isotopic signal. River simulations were run as batch simulations (no flow) assuming that the suspended load is transported at the same velocity as river water. Moreover, river simulations consider a diffusive dilution of the exfiltrated groundwater with water that experienced no previous water–rock interaction (i.e., pure water +  $\text{CO}_2$ ). For both systems (subsurface and river), Li isotopic fractionation is simulated to occur during kaolinite and goethite precipitation.

**Table 1**  
Initial and boundary conditions.

		Simulation of current weathering pattern		Simulation of Paleocene–Eocene boundary weathering pattern	
		Subsurface	River	“Fresh granite”	“Altered granite”
pH	–	5.63	<sup>a</sup> 8.79	5.37	5.37
HCO <sub>3</sub> <sup>–</sup>	mol/kg <sub>H2O</sub>	<sup>b</sup> 1.51E–5	<sup>a</sup> 4.18E–3	<sup>c</sup> 4.52E–05	<sup>c</sup> 4.52E–05
Na <sup>+</sup>	mol/kg <sub>H2O</sub>	1.0E–10	<sup>a</sup> 3.45E–6	1.0E–10	1.0E–10
K <sup>+</sup>	mol/kg <sub>H2O</sub>	1.0E–10	<sup>a</sup> 1.67E–4	1.0E–10	1.0E–10
Mg <sup>2+</sup>	mol/kg <sub>H2O</sub>	1.0E–10	<sup>a</sup> 2.00E–5	1.0E–10	1.0E–10
Ca <sup>2+</sup>	mol/kg <sub>H2O</sub>	1.0E–10	<sup>a</sup> 2.22E–3	1.0E–10	1.0E–10
Al <sup>3+</sup>	mol/kg <sub>H2O</sub>	1.0E–10	<sup>a</sup> 8.31E–7	1.0E–10	1.0E–10
<sup>6</sup> Li <sup>+</sup>	mol/kg <sub>H2O</sub>	<sup>d</sup> 7.68095E–11	<sup>a</sup> 4.5097E–8	<sup>d</sup> 7.68095E–11	<sup>d</sup> 7.68095E–11
<sup>7</sup> Li <sup>+</sup>	mol/kg <sub>H2O</sub>	<sup>d</sup> 9.23191E–10	<sup>a</sup> 5.4726E–7	<sup>d</sup> 9.23191E–10	<sup>d</sup> 9.23191E–10
SiO <sub>2(aq)</sub>	mol/kg <sub>H2O</sub>	1.0E–10	<sup>a</sup> 3.36E–4	1.0E–10	1.0E–10
O <sub>2(aq)</sub>	mol/kg <sub>H2O</sub>	2.5E–4	2.5E–4	2.5E–4	2.5E–4
Fe <sup>2+</sup>	mol/kg <sub>H2O</sub>	1.0E–10	<sup>a</sup> 6.59E–19	1.0E–10	1.0E–10
CO <sub>2(s)</sub>	Vol frac (of solids)	0.01	0.01	0.01	0.01
Albite	Vol frac (of solids)	0.304	0.304	0.304	0.304
Anorthite	Vol frac (of solids)	0.076	0.076	0.076	0.076
Orthoclase	Vol frac (of solids)	0.29	0.29	0.29	0.29
Quartz	Vol frac (of solids)	0.31	0.31	0.31	0.31
Annite	Vol frac (of solids)	0.04	0.04	0.04	0.04
Li-phlogopite	Vol frac (of solids)	0.01	0.01	0.01	0.01
Kaolinite	Vol frac (of solids)	0.0	0.0	0.0	0.004 <sup>e</sup>
<sup>6</sup> Li (kaolinite)	Vol frac (of solids)	0.0	0.0	0.0	0.00031020 <sup>e</sup>
<sup>7</sup> Li (kaolinite)	Vol frac (of solids)	0.0	0.0	0.0	0.00368979 <sup>e</sup>
Goethite	Vol frac (of solids)	0.0	0.0	0.0	0.0003 <sup>e</sup>
<sup>6</sup> Li (kaolinite)	Vol frac (of solids)	0.0	0.0	0.0	0.00002326 <sup>e</sup>
<sup>7</sup> Li (kaolinite)	Vol frac (of solids)	0.0	0.0	0.0	0.00027673 <sup>e</sup>
Porosity	–	0.1	0.99	0.1	0.1

<sup>a</sup> Read out from downstream boundary of subsurface model run.

<sup>b</sup> Calculated by assuming equilibrium with pCO<sub>2</sub> of 370 ppmV (log(pCO<sub>2</sub>) = –3.43).

<sup>c</sup> Calculated by assuming equilibrium with pCO<sub>2</sub> of 1200 ppmV (log(pCO<sub>2</sub>) = –2.92).

<sup>d</sup> Specification corresponds to an initial δ<sup>7</sup>Li of 0.0‰.

<sup>e</sup> Read out from model run with “fresh granite” domain only.

fitting parameters that must be experimentally determined. For this study they were taken as equal to one, which is usually, but not always the case. In order to calculate effective precipitation and dissolution rates (Eq. (3)) reaction rate constants were defined according to Palandri and Kharaka (2004) whereas equilibrium constants were taken from the Soltherm.H06 database (Reed and Palandri, 2006), which was derived using SUPCRT92 (Johnson et al., 1992). Mineral stoichiometries, thermodynamic and kinetic parameters, and initial mineral and fluid compositions are summarized in Tables 1 and 2.

### 3.1.2. River simulations

River simulations were conducted essentially as batch simulations, where the flow velocity was set to zero (Fig. 2). In doing so, it was assumed that the reactive suspended load (i.e., solid phase) is transported at the same velocity as river water, which is in agreement with current knowledge about transport of suspended river loads (Fryirs and Brierley, 2013). Simulating reactive transport in rivers by means of a batch simulation is justified because only the relative transport velocity between aqueous and solid phases (i.e., suspended load) matters, whereas the actual velocity of the two phases has no effect as long as aqueous and solid phases are transported at the same velocity.

Two grid blocks of 1 × 1 × 1 m each were defined to simulate that subsurface waters exfiltrating into river systems are diluted by river water, which previously experienced no or only minor water–rock interaction. Consequently, steady-state concentrations obtained at the downstream model boundary of the subsurface simulations were taken as input concentrations for one of the two grid blocks, while pure water in equilibrium with CO<sub>2</sub> was defined as the initial concentration for the second grid block (Fig. 2). It should be noted, that this particular grid block has no geochemical meaning other than ensuring that exfiltrated subsurface water is diluted during its transport in the

river. Due to the initial concentration gradient, a diffusive flux J<sub>D<sub>i</sub></sub> occurred between the two grid blocks, expressed as

$$J_{D_i} = \frac{\Phi \cdot \tau \cdot D_{aq} \cdot A_{Interface}}{d_1 + d_2} \cdot \frac{dC_i}{dx} \quad (4)$$

where D<sub>aq</sub> refers to the molecular diffusion coefficient of aqueous species (~10<sup>–9</sup> m<sup>2</sup>/s), A<sub>Interface</sub> (m<sup>2</sup>) is the interfacial area between the two grid blocks, dC<sub>i</sub>/dx (mol/kg<sub>H2O</sub>/m) is the concentration gradient of species i, d<sub>1</sub> and d<sub>2</sub> (m) refer to the distances from the center of the two grid blocks to their mutual interface, and Φ and τ are the porosity and tortuosity, respectively. Reactions between the suspended river load and river waters were only considered for the grid block initially containing exfiltrating subsurface water. By setting the corresponding porosity to a very large value of 99.9% (Fig. 2), it was ensured that the suspended load only forms a minor fraction of the total river volume. The tortuosity was set to 1.0 for both grid blocks.

The same initial granitic mineralogical composition as for the subsurface “fresh granite” domain was assigned to the suspended river load (Table 1). In doing this, we assume that the suspended load contains a significant amount of primary silicate minerals in addition to the dominant clays and oxides (Gaillardet et al., 1999). This model assumption is consistent with Bouchez et al. (2011) who observed that the mineralogical composition of the suspended load is dependent on the particle size and that primary silicate minerals (e.g., quartz, albite) are enriched in the coarser fraction. Consequently, new goethite and kaolinite are allowed to precipitate and Li isotopic fractionation in the simulated river thus occurs in the same fashion as in the subsurface simulations. As long as primary silicate minerals are exposed to chemical weathering, our river simulations are not sensitive to the ratio between primary and secondary minerals. Accordingly, we did not change the initial mineral volume fraction when compared to the subsurface simulations (Table 1).

**Table 2**  
Simulated silicate weathering reactions.

Mineral phase	<sup>a</sup> log(K)	<sup>b</sup> k (mol/m <sup>2</sup> /s)	<sup>c</sup> A <sup>fresh granite</sup> (cm <sup>2</sup> /g)	<sup>c</sup> A <sup>altered granite</sup> (cm <sup>2</sup> /g)	<sup>c</sup> A <sup>river simulation</sup> (cm <sup>2</sup> /g)	Hydrolysis reaction
CO <sub>2(s)</sub> <sup>d</sup>	-11.25	1.00e-04	100	100	100	CO <sub>2(s)</sub> + H <sub>2</sub> O = H <sup>+</sup> + HCO <sub>3</sub> <sup>-</sup>
Albite <sup>e1</sup>	1.41	2.75E-13	1	0	6000 or 375 <sup>f</sup>	NaAlSi <sub>3</sub> O <sub>8</sub> + 4H <sup>+</sup> = Na <sup>+</sup> + 3SiO <sub>2(aq)</sub> + Al <sup>3+</sup> + 2H <sub>2</sub> O
Anorthite <sup>e1</sup>	24.52	7.59E-10	1	0	6000 or 375	CaAl <sub>2</sub> Si <sub>2</sub> O <sub>8</sub> + 8H <sup>+</sup> = Ca <sup>2+</sup> + 2SiO <sub>2(aq)</sub> + 3Al <sup>3+</sup> + 4H <sub>2</sub> O
Orthoclase	-0.20	3.89E-13	1	0	6000 or 375	KAlSi <sub>3</sub> O <sub>8</sub> + 4H <sup>+</sup> = K <sup>+</sup> + 3SiO <sub>2(aq)</sub> + Al <sup>3+</sup> + 2H <sub>2</sub> O
Quartz	-4.05	2.46E-13	1	0	6000 or 375	SiO <sub>2(s)</sub> = SiO <sub>2(aq)</sub>
Annite <sup>e2</sup>	29.37	3.16E-11	2.4	0	6000 or 375	KFe <sub>3</sub> AlSi <sub>3</sub> O <sub>10</sub> (OH) <sub>2</sub> + 10H <sup>+</sup> = Al <sup>3+</sup> + K <sup>+</sup> + 3Fe <sup>2+</sup> + 6H <sub>2</sub> O + 3SiO <sub>2</sub>
Li-phlogopite <sup>e2,g</sup>	37.43	3.98E-13	2.4	0	6000 or 375	K <sub>1.144</sub> Mg <sub>2.856</sub> Li <sub>0.144</sub> (AlSi <sub>3</sub> O <sub>10</sub> )(OH) <sub>2</sub> + 10H <sup>+</sup> = 1.144 K <sup>+</sup> + 2.856 Mg <sup>2+</sup> + 0.01104322 <sup>6</sup> Li <sup>+</sup> + 0.13295678 <sup>7</sup> Li <sup>+</sup> + Al <sup>3+</sup> + 3SiO <sub>2(aq)</sub>
Kaolinite <sup>e3</sup>	7.55	6.6E-14	6824	6824	6000 or 375	Al <sub>2</sub> Si <sub>2</sub> O <sub>5</sub> (OH) <sub>4</sub> + 6H <sup>+</sup> = 2Al <sup>3+</sup> + 2SiO <sub>2(aq)</sub> + 5H <sub>2</sub> O
<sup>6</sup> Li (kaolinite) <sup>e3,h</sup>	-2.60877392	6.6E-14	6824	6824	6000 or 375	<sup>6</sup> Li = <sup>6</sup> Li <sup>+</sup>
<sup>7</sup> Li (kaolinite) <sup>e3,h</sup>	-2.6	6.6E-14	6824	6824	6000 or 375	<sup>7</sup> Li = <sup>7</sup> Li <sup>+</sup>
Goethite <sup>e4</sup>	-8.3710	1.15E-8	6824	6824	6000 or 375	Fe(OH) <sub>3</sub> + 2H <sup>+</sup> = 0.25O <sub>2(aq)</sub> + 1.5H <sub>2</sub> O + Fe <sup>2+</sup>
<sup>6</sup> Li (goethite) <sup>e4,h</sup>	-2.60877392	1.15E-8	6824	6824	6000 or 375	<sup>6</sup> Li = <sup>6</sup> Li <sup>+</sup>
<sup>7</sup> Li (goethite) <sup>e4,h</sup>	-2.6	1.15E-8	6824	6824	6000 or 375	<sup>7</sup> Li = <sup>7</sup> Li <sup>+</sup>

<sup>a</sup> With the exception of kaolinite, which was defined according to Yang and Steefel (2008), equilibrium constants log(K) were defined according to Reed and Palandri (2006).  
<sup>b</sup> Reaction rate constants k were defined according to Palandri and Kharaka (2004).  
<sup>c</sup> Reactive surface areas of primary silicate minerals (feldspars, quartz, biotite) were calibrated to get a Li concentration larger than the global average riverine Li conc. (0.265 μmol/L) at the downstream aquifer model boundary ("mixing", Fig. 2). Reactive surface areas of secondary minerals (e.g., kaolinite, goethite) were set to 6824 cm<sup>2</sup>/g according to Dobson et al. (2003).  
<sup>d</sup> Hypothetical solid CO<sub>(s)</sub> phase to fix pCO<sub>2</sub> (= model CO<sub>2</sub> source). Different values were defined to fix pCO<sub>2</sub> to 1200 ppmV (log(K) = -10.739) and 370 ppmV (log(K) = -11.252).  
<sup>e</sup> Endmember of solid solution x.  
<sup>f</sup> River simulations were run for two different reactive surface areas to simulate the effects of a varying suspended river load on riverine δ<sup>7</sup>Li values. 6000 cm<sup>2</sup>/g allowed matching the current global average riverine δ<sup>7</sup>Li value after a simulated river residence time of 20 days.  
<sup>g</sup> Corresponds to a phlogopite Li concentration of 2400 ppm to get an initial bulk granite Li conc. of 24 ppm according to Economos (2010) (at a phlogopite vol fraction of 0.01), and a δ<sup>7</sup>Li value of 0.0‰.  
<sup>h</sup> Li isotopic endmember of defined solid solution (Fig. 3). K<sub>6Li</sub>/K<sub>7Li</sub> = 0.98 = Δ<sup>7</sup>Li<sub>solution-kaolinite</sub> = -20‰. log(K) was calibrated to get maximum Li concentration in goethite and kaolinite of about 200 ppm.

3.2. Simulation of Li isotopic fractionation

To simulate Li isotopic fractionation, <sup>6</sup>Li and <sup>7</sup>Li were incorporated into the mineral stoichiometries of biotite, kaolinite and goethite (Table 2). An initial δ<sup>7</sup>Li value of 0.0‰ was assumed for Li-bearing biotite corresponding to the average δ<sup>7</sup>Li value of the upper continental crust (Teng et al., 2004). Assuming stoichiometric biotite dissolution, our simulations agree with previous studies showing that no or only minor Li isotopic fractionation occurs during mineral dissolution (Pistiner and Henderson, 2003; Huh et al., 2004). In contrast, our model considers Li isotopic fractionation during Li incorporation into precipitating kaolinite and goethite, using a solid solution approach similar to the one described for simulating Sr and Cr isotopic fractionation (Sonnenthal et al., 1998; Wanner and Sonnenthal, 2013). It should be noted, however, that Li must be treated slightly differently because it is incorporated into secondary minerals as a trace element, whereas Cr and Sr can be major constituents of minerals controlling the fate of Cr and Sr isotopes (e.g., Cr(OH)<sub>3</sub> and SrCO<sub>3</sub>). Particularly challenging is the fact that, although some suggestions are found in the literature (Pistiner and Henderson, 2003; Vigier et al., 2008), it has not yet been shown how Li structurally substitutes into kaolinite and goethite. Because of this lack of detailed mineralogical knowledge, our model assumes a solid solution with three different endmembers (Fig. 3) to simulate Li uptake and associated Li isotopic fractionation during kaolinite and goethite precipitation: (i) a pure, non-Li bearing kaolinite and goethite endmember, (ii) a pure <sup>6</sup>Li bearing mineral endmember and (iii) a pure <sup>7</sup>Li bearing endmember. The pure <sup>6</sup>Li and <sup>7</sup>Li endmembers are hypothetical, but their specification allows fitting experimentally observed aqueous Li concentrations as well as measured amounts of Li that are incorporated in secondary minerals by calibrating the corresponding log(K) values.

The precipitation rate r<sub>prec</sub> of the Li bearing kaolinite and goethite solid solution is defined as the sum of the individual endmember (Fig. 3) precipitation rates r<sub>pure2nd</sub>, r<sub>6Li</sub> and r<sub>7Li</sub>:

$$r_{prec} = r_{pure2nd} + r_{6Li} + r_{7Li} \tag{5}$$

The rate of a specific endmember, r<sub>endm</sub>, is calculated according to a TST-like expression

$$r_{endm} = A \cdot k \cdot \left(1 - \frac{Q_{endm}}{K_{endm}}\right) + k \cdot A \cdot (x_{endm} - 1) \tag{6}$$

where x<sub>endm</sub> refers to the mole fraction of a specific secondary mineral endmember. For the hypothetical, pure <sup>6</sup>Li and <sup>7</sup>Li endmembers x<sub>6Li</sub> and x<sub>7Li</sub> are calculated according to:

$$x_{6Li} = \frac{Q_{6Li}/K_{6Li}}{Q_{6Li}/K_{6Li} + Q_{7Li}/K_{7Li}} \tag{7}$$

$$x_{7Li} = \frac{Q_{7Li}/K_{7Li}}{Q_{6Li}/K_{6Li} + Q_{7Li}/K_{7Li}} \tag{8}$$

Eqs. (7) and (8) ensure that the amount of Li that is incorporated into goethite and kaolinite reflects the Li concentration of the aqueous solution. Accordingly, the amount of Li removed by precipitation

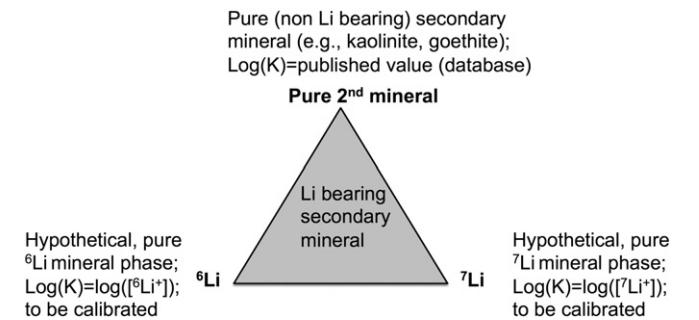


**Fig. 3.** Schematic illustration of the composition of modeled Li bearing secondary minerals, which were simulated as ideal solid solutions. The three endmembers were defined as pure goethite or kaolinite with known thermodynamic properties, and hypothetical, but pure <sup>6</sup>Li and pure <sup>7</sup>Li, for which log(K) values have to be calibrated by matching observed secondary mineral and aqueous Li concentrations.

increases with increasing aqueous Li concentration. By doing so, our model is in good agreement with an experimental study showing that [Li] of synthesized smectites is linearly correlated with the corresponding aqueous [Li] (Decarreau et al., 2012).

Using the solid solution approach described above allows conveniently specifying a particular Li isotopic fractionation factor  $\alpha$  and corresponding enrichment factor  $\varepsilon$  for our simulations:

$$\alpha = \frac{K_6\text{Li}}{K_7\text{Li}} \quad (9)$$

$$\varepsilon = (\alpha - 1) \cdot 1000 \approx \Delta^7\text{Li} = \delta^7\text{Li}_{2\text{ndMin}} - \delta^7\text{Li}_{\text{solution}} \quad (10)$$

Experimentally-determined Li isotopic enrichment factors for Li incorporation into precipitating minerals have so far only been reported for smectite, yielding values between  $-1.6$  (at  $T = 250$  °C) and  $-16.5\%$  (at  $T = 25$  °C), depending on the experimental temperature (Vigier et al., 2008; personal communication). Other studies determined  $\Delta^7\text{Li}$  values between dissolved and suspended Li loads in rivers yielding  $\Delta^7\text{Li}_{\text{suspended-dissolved}}$  from  $-6$  to  $-36\%$  (Huh et al., 2001; Kisakürek et al., 2005; Pogge von Strandmann et al., 2006, 2010). Because of this relatively sparse dataset, we assigned a Li isotopic enrichment factor of  $-20\%$  for kaolinite as well as for goethite precipitation, which is within the range of Li isotopic enrichment factors reported or inferred for secondary mineral precipitation.

Li adsorption on solid surfaces has been proposed as an additional process causing Li isotopic fractionation (Zhang et al., 1998; Pistiner and Henderson, 2003). Significant fractionation ( $\varepsilon = -13\%$ ) was reported for an experiment involving Li adsorption via surface complexation reactions at gibbsite surfaces (Pistiner and Henderson, 2003). Moreover, enrichment factors of  $-21\%$  and  $-29\%$  were experimentally determined for Li adsorption on kaolinite and vermiculite, respectively (Zhang et al., 1998). These enrichment factors, however, were determined by solely studying the dissolved Li and no information regarding the surface complexation or substitution reaction is available. In contrast, very little Li isotopic fractionation was observed during Li exchange (i.e., ion exchange reaction) with smectite interlayers (Pistiner and Henderson, 2003; Vigier et al., 2008). Overall, experimental data suggest that Li isotopic fractionation is caused by surface complexation reactions associated with a changing Li coordination chemistry or by Li substitution into crystal lattices. In contrast, physical Li adsorption by ion exchange reactions does not seem to cause significant fractionation. Similar to Bouchez et al. (2013) our model does not distinguish between Li exchange-, Li surface complexation-, or Li substitution reactions and Li uptake by secondary minerals and associated Li isotopic fractionation is solely simulated as a crystallographic substitution reaction during the formation of kaolinite and goethite such as discussed earlier.

Li isotope fractionation inherited from differences in the aqueous  $^6\text{Li}$  and  $^7\text{Li}$  diffusive flux was neglected because kaolinite and goethite precipitation was not assumed to be transport-limited by Li diffusion.

## 4. Model results and discussion

### 4.1. Simulation of the current weathering pattern (Fig. 1b)

To simulate the inferred current weathering pattern with predominant weathering of primary silicate minerals (Fig. 1) a “fresh granite” mineralogical composition was assigned to the entire subsurface model domain (i.e., 100% “fresh granite”) and the  $p\text{CO}_2$  was fixed to the approximate current atmospheric  $p\text{CO}_2$  of ca. 370 ppm volume (ppmV) (Keeling, 1960). The solubility of the pure, but hypothetical Li-bearing kaolinite and goethite endmember ( $\log(K)$ ) was calibrated to  $-2.6$  (Table 2) to get a maximum kaolinite and goethite Li

concentration within the subsurface domain of 200 ppm. A maximum value of 200 ppm is in agreement with Li concentration measurements in continental clays (Tardy et al., 1972). For the subsurface simulations, reactive surface areas for primary mineral phases were set to  $1\text{--}2$   $\text{cm}^2/\text{g}$  (Table 2) to obtain a Li concentration at the end of the subsurface domain ( $4.08$   $\mu\text{g}/\text{L}$ , Fig. 4a, d) that is larger than the global average riverine value of  $1.83$   $\mu\text{g}/\text{L}$  (Misra and Froelich, 2012). A reactive surface area of  $1\text{--}2$   $\text{cm}^2/\text{g}$  also ensured that chemical equilibrium was not fully established within the subsurface domain and that primary mineral dissolution was occurring along the full domain (Fig. 4b, e). Reactive surface areas of precipitating kaolinite and goethite were set to the high value of  $6824$   $\text{cm}^2/\text{g}$  based on Dobson et al. (2003).

With the specified parameters, our model yielded a continuous  $\delta^7\text{Li}$  increase along the subsurface model domain reaching a dissolved  $\delta^7\text{Li}$  value of roughly  $+10\%$  at the downstream model boundary (Fig. 4a, d). It should be noted that the slope of the  $\delta^7\text{Li}$  increase with residence time is dependent on the specified enrichment factor. For lower factors (i.e., less fractionation), longer residence time is needed to reach the same  $\delta^7\text{Li}$  as for  $\varepsilon = -20\%$ , or vice versa. However, the correlation between  $\delta^7\text{Li}$  and residence time is not sensitive to the specified enrichment factor. A  $\delta^7\text{Li}$  value of  $+10\%$  is significantly lower than the current global average riverine  $\delta^7\text{Li}$  value of  $+23\%$  (Misra and Froelich, 2012) implying that Li isotopic fractionation occurring in rivers forms a major contribution on riverine  $\delta^7\text{Li}$ . This simulation finding is supported by  $\delta^7\text{Li}$  values derived from groundwaters and rivers draining the Columbia River basalt as well as small granitic catchments yielding significantly larger  $\delta^7\text{Li}$  values for river samples (Lemarchand et al., 2010; Liu et al., in revision). Consequently, the reactive surface area of the suspended river load  $A_{\text{suspended\_load}}$  was calibrated to  $6000$   $\text{cm}^2/\text{g}$  (Table 2) for the corresponding river simulation to match the global average riverine  $\delta^7\text{Li}$  value ( $+23\%$ ) after a simulated river residence time of 20 days, for which all river simulations were run (Fig. 4a). Similarly, the interfacial area between the two grid blocks of the river simulation  $A_{\text{interface}}$  (Eq. (4), Fig. 2) was set to  $2560$   $\text{m}^2$  to result in dilution of the exfiltrated groundwater by a factor of roughly 2. In doing so, the obtained Li concentration at the end of the river simulation ( $0.79$   $\mu\text{g}/\text{L}$ , Fig. 4a) was somewhat lower but still in the same order of magnitude as the global average riverine Li concentration of  $1.83$   $\mu\text{g}/\text{L}$  (Misra and Froelich, 2012).

To explore the sensitivity of riverine  $\delta^7\text{Li}$  on the reactivity of the suspended river load and thus on the actual suspended load concentration, the river simulation was also performed for an  $A_{\text{suspended\_load}}$  of  $375$   $\text{cm}^2/\text{g}$  (Table 2). This value is 16 times lower than the initial surface area ( $6000$   $\text{cm}^2/\text{g}$ ), and thus corresponds to the Misra and Froelich (2012) interpretation proposing that “the riverine Li flux has changed the ratio of dissolved to suspended partitioning from 4:1 in Paleocene to 1:4 today”. Simulation results show that only minor Li isotopic fractionation takes place if the reactivity of the suspended load is this low (Fig. 4d). The high sensitivity of riverine  $\delta^7\text{Li}$  on  $A_{\text{suspended\_load}}$  implies that an increasing suspended river load concentration may have formed an important contribution on the seawater and global average riverine  $\delta^7\text{Li}$  increase observed during the Cenozoic (Misra and Froelich, 2012).

Our simulation results also imply that riverine  $\delta^7\text{Li}$  values increase with increasing subsurface residence time (Fig. 4a, d). This particular finding is in good agreement with seasonal riverine  $\delta^7\text{Li}$  variations observed in streams draining the Columbia river basalt west of the Cascade Range, where seasonal precipitation and thus subsurface residence time variations are large (Liu et al., in revision). It is, however, unlikely that a Cenozoic global average subsurface residence time increase caused the Cenozoic seawater  $\delta^7\text{Li}$  increase because for an increasing relief (e.g., over the Cenozoic), residence times tend to decrease and not to increase.

### 4.2. Simulation of the Paleocene–Eocene boundary weathering pattern (Fig. 1a)

A series of simulations with a varying “fresh granite” volume fraction corresponding to a varying contribution of “fresh granite” weathering

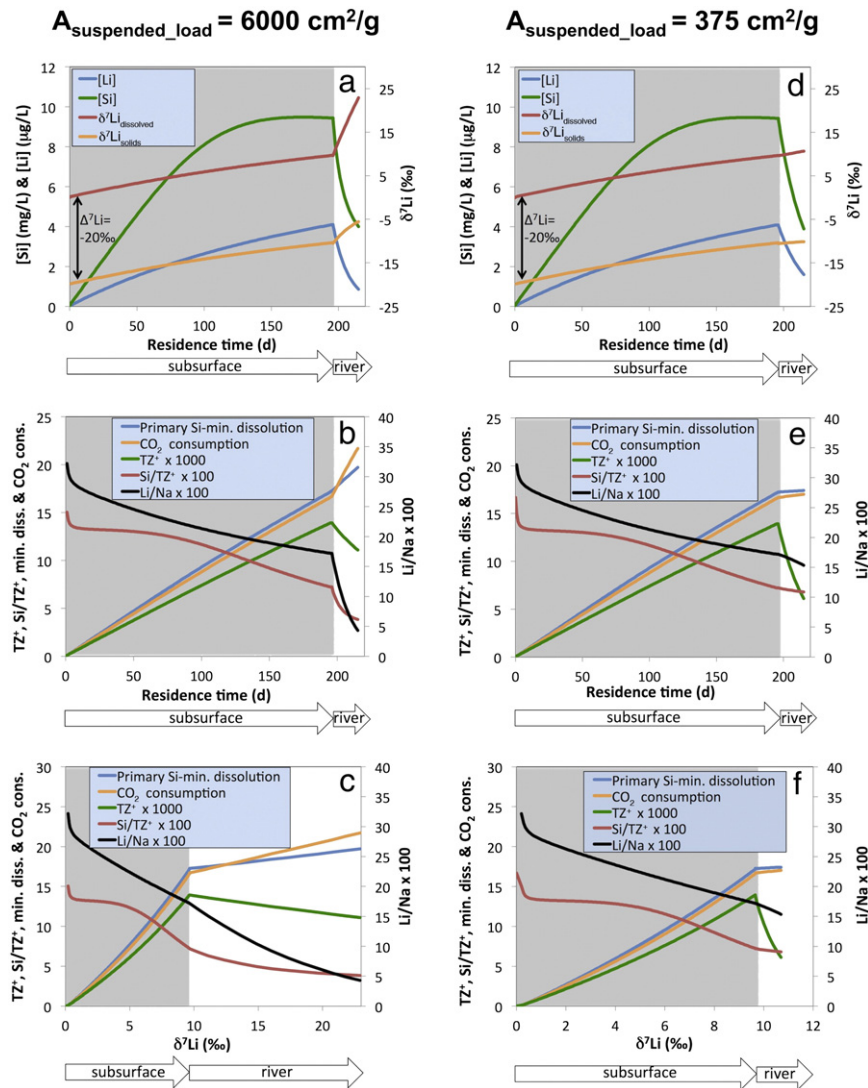


**Fig. 4.** Model results for the simulated current weathering pattern with 100% “fresh granite” contribution (Fig. 1b). (a) and (d) illustrate steady state [Li] and [Si] along the full model domain (subsurface + river), as well as corresponding  $\delta^7\text{Li}$  profiles ( $\delta^7\text{Li}_{\text{dissolved}}$  and  $\delta^7\text{Li}_{\text{kaolinite}} = \delta^7\text{Li}_{\text{goethite}} = \delta^7\text{Li}_{\text{solids}}$ ) for a reactive suspended river load surface area of 6000 cm<sup>2</sup>/g and 375 cm<sup>2</sup>/g, respectively, illustrating that the simulated  $\Delta^7\text{Li}_{\text{solids-dissolved}}$  was equal to the initially specified Li isotope enrichment factor of  $\epsilon = -20\text{‰}$ . (b) and (e) present corresponding steady state profiles of typical silicate weathering tracers such as TZ<sup>+</sup> (in meqv/kg), Si/TZ<sup>+</sup>, Li/TZ<sup>+</sup> and Li/Na (molar ratio). Also shown are the cumulative primary mineral dissolution (quartz + feldspars + biotite) and corresponding CO<sub>2</sub> consumption profiles (in kmol) during a simulated time period of 100 years. (c) and (f) illustrate the relationship between the parameters shown in (b) and (e) as a function of  $\delta^7\text{Li}_{\text{dissolved}}$ . Note that profiles except the ones shown in (c) and (f) are plotted against fluid residence time to simultaneously illustrate subsurface and river simulations. Along the subsurface domain (gray shaded area) fluid residence time (x-axis) also corresponds to the distance along the subsurface domain because the flow velocity was 1 m/d.

(i.e., varying weathering intensity) was run to match riverine  $\delta^7\text{Li}$  values inferred for the Paleocene–Eocene boundary. These simulations were run for a fixed  $p\text{CO}_2$  of 1200 ppmV to account for the atmospheric  $p\text{CO}_2$  inferred for the Paleocene–Eocene boundary (Li and Elderfield, 2013). For the “altered granite” domain the reactive surface area of primary silicates was set to zero, thus simulating an extreme weathering intensity where primary minerals are either fully replaced or fully coated by secondary minerals. Moreover, the initial presence of Li-bearing kaolinite and goethite was specified for this model domain, whereas their Li isotopic composition and initial volume fractions (e.g.,  $\delta^7\text{Li} = -10\text{‰}$ , Table 1) were input from the results of a pure “fresh granite” run (i.e., 100% “fresh granite”) after a simulated time period of 100 years. In contrast to the runs simulating the current weathering pattern, the varying weathering intensity runs were only performed for the subsurface domain (Fig. 2) because our simulation results imply that only minor Li isotopic fractionation occurs within rivers where the suspended river load concentration is low (Fig. 4d), which

has been inferred for the Paleocene–Eocene boundary (Misra and Froelich, 2012).

Model results show that downstream  $\delta^7\text{Li}$  values become more positive with an increasing contribution of “fresh granite” weathering (i.e., decreasing weathering intensity) (Fig. 5a). A strong correlation between  $\delta^7\text{Li}$  and fresh granite is, however, only observed for fresh granite contributions <10%, which is inherited from the strong Li solubility contrast between the “fresh granite” (i.e., Li-bearing biotite) and the “altered granite” domain (i.e., Li bearing kaolinite and goethite) (Fig. 6). Nevertheless, our simulations imply that a decreasing weathering intensity over the Cenozoic may have formed an important contribution to the Cenozoic seawater and global average riverine  $\delta^7\text{Li}$  increase (Misra and Froelich, 2012) in addition to the increasing suspended river load concentration (Fig. 4a, d). Moreover, our simulations show that low global average riverine  $\delta^7\text{Li}$  values inferred for the Paleocene–Eocene boundary (Misra and Froelich, 2012) may have been inherited from predominant dissolution of previously formed secondary



mineral phases having a low  $\delta^7\text{Li}$  value (e.g.,  $-10\%$ , Fig. 6a) and a minor contribution of primary silicate rock dissolution and corresponding precipitation of newly formed secondary mineral phases associated with Li isotopic fractionation. For our simplified system (Fig. 2), a fresh granite contribution of about 5% is required to obtain a  $\delta^7\text{Li}$  value similar to the minimum value inferred for the Paleocene–Eocene boundary at the downstream subsurface model boundary (e.g.,  $+6\%$ , Fig. 5a). It should be noted that this particular interpretation is entirely different from the one of Misra and Froelich (2012) because it does not rely on congruent weathering of primary silicate minerals.

#### 4.2.1. Model uncertainty and mass balance considerations

If a significant proportion of Li was adsorbed to goethite and kaolinite surfaces rather than fully substituted into the crystal structure, Li solubility of weathering-intense, secondary mineral dominated systems could be much higher than shown in Fig. 6a. Especially for estuaries where the ionic strength is higher than it is in aquifers or rivers, Li complexed to kaolinite and goethite surfaces could be readily desorbed by surface complexation reactions involving other, highly concentrated cations (e.g., Na, K, Ca, Mg). Such estuarine desorption has been shown for various other trace metals (Du Laing et al., 2009).

Distinguishing between Li surface complexation and Li substitution reactions in our model would simply change the slope and curvature of the  $\delta^7\text{Li}$  vs. weathering intensity relation (Fig. 5a). Consequently, it would also change the amount of fresh granite weathering that is required to obtain an inferred  $\delta^7\text{Li}$  value of  $+6\%$ . The same applies if we were using a Li isotopic enrichment factor other than  $-20\%$ , or if exchanged/complexed Li did not show the same  $\delta^7\text{Li}$  value than structural Li, which was observed for Mg (Wimpenny et al., 2014). However, our main model observations, the overall inverse correlation between weathering intensity and riverine  $\delta^7\text{Li}$  would remain unchanged (Fig. 5a).

The above discussion illustrates that riverine [Li] derived from our model should be considered as an end-member, minimum [Li] scenario for the Paleocene–Eocene boundary ([Li] =  $0.25 \mu\text{g/L}$ , Fig. 5a). Updating the Misra and Froelich (2012) mass balance calculation with this [Li] as well as the inferred minimum riverine  $\delta^7\text{Li}$  ( $+6\%$ ) yields seawater  $\delta^7\text{Li}$  and [Li] of  $+24\%$  and  $112 \mu\text{g/L}$ , respectively. Whereas the calculated seawater  $\delta^7\text{Li}$  is close to the observed value ( $+22\%$ , Misra and Froelich, 2012),  $112 \mu\text{g/L}$  is significantly lower than the inferred Paleocene–Eocene seawater [Li] ( $179 \mu\text{g/L}$ ), which is based on the

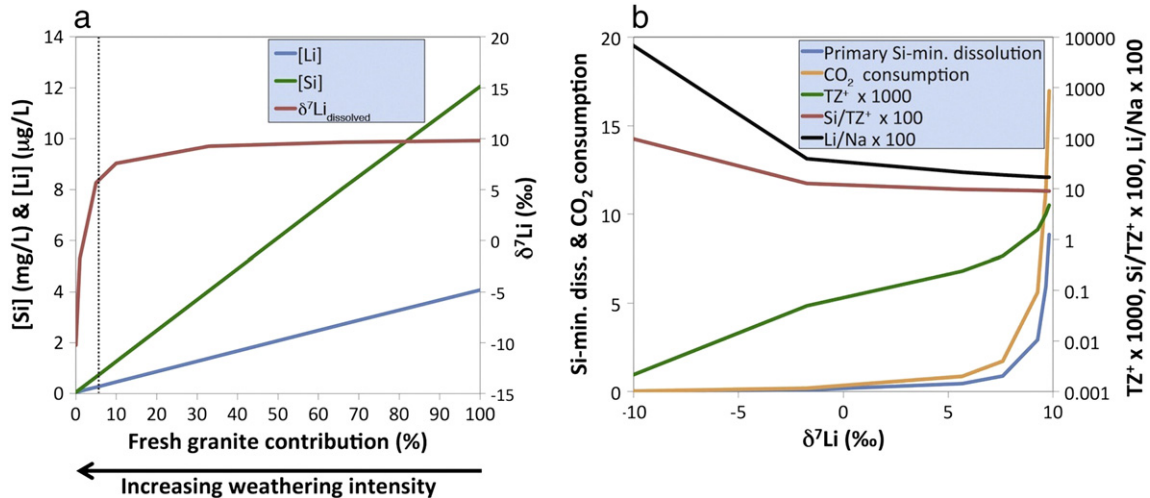


Fig. 5. Model results for the simulated Paleocene–Eocene boundary weathering pattern (Fig. 1a). (a) Steady state [Si], [Li] and  $\delta^7\text{Li}$  at the downstream subsurface model boundary ("mixing", Fig. 2) plotted as a function of the simulated "fresh granite" contribution or inverse weathering intensity, respectively. The dashed line illustrates that 5% fresh granite contribution is required to get an assumed Paleocene–Eocene boundary riverine  $\delta^7\text{Li}$  value of  $+6\%$ , which in turn yields a corresponding [Li] of  $0.25 \mu\text{g/L}$ . (b) Cumulative amounts of primary mineral dissolution (feldspars, biotite, quartz) and  $\text{CO}_2$  consumption (in kmol) within the entire subsurface model domain during a simulated time period of 100 years as a function of steady state  $\delta^7\text{Li}$  values at the downstream subsurface model boundary. Also shown are steady state  $\text{TZ}^+$  (in meq/kg),  $\text{Si}/\text{TZ}^+$  and  $\text{Li}/\text{Na}$  (molar ratio) at the downstream subsurface model boundary as a function of corresponding  $\delta^7\text{Li}$  values.

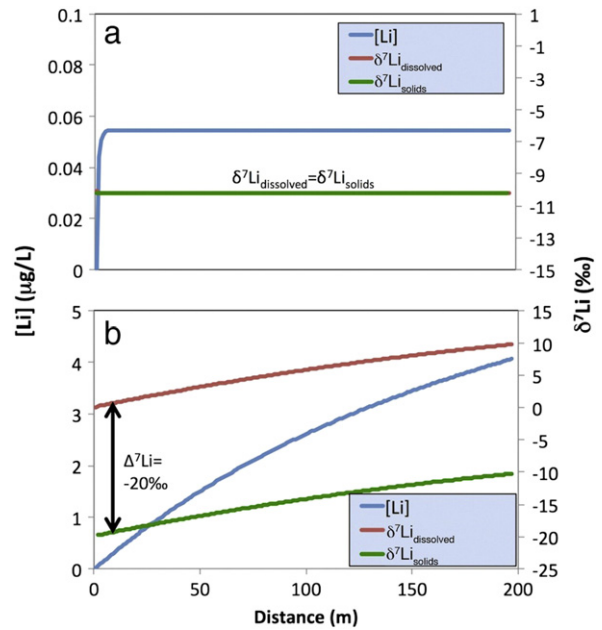


Fig. 6. Simulated steady-state [Li] and  $\delta^7\text{Li}$  profiles along the altered (a) and fresh granite domain (b) of the Paleocene–Eocene boundary weathering pattern (Fig. 1a).

assumption that seawater [Li] remained constant throughout the Cenozoic (Misra and Froelich, 2012). If seawater [Li] was indeed constant, the contradiction with the updated mass balance calculation could be resolved by increasing the hydrothermal Li flux by a factor of about 1.6 or by increasing continental discharge by a factor of ca. 7.3, both having only a minor effect on seawater  $\delta^7\text{Li}$  ( $<1\%$ ). However, only the hydrothermal [Li] flux increase seems to be in a reasonable order of magnitude (Otto-Bliesner, 1995; Berner and Kothavala, 2001).

When discussing mass balance calculations for the global Li cycle it should be noted that the calculations performed by Misra and Froelich (2012) are highly sensitive to Li isotopic fractionation occurring in the ocean during Li uptake by pelagic sediments and alteration of the basaltic oceanic crust (i.e., reverse weathering). For oceanic Li isotopic fractionation to cause a seawater  $\delta^7\text{Li}$  shift less than  $+16\%$ , the Paleocene–Eocene boundary mass balance also works (i.e., seawater

$\delta^7\text{Li} = +22\%$ ) for riverine  $\delta^7\text{Li}$  and/or  $[\text{Li}]$  (i.e., Li flux) larger than the ones derived from our end-member considerations ( $[\text{Li}] = 0.25 \mu\text{g/L}$ ,  $\delta^7\text{Li} = +6\%$ , Fig. 5a).

In summary, a reasonable mass balance can be formulated with riverine  $[\text{Li}]$  and  $\delta^7\text{Li}$  derived from our model ( $[\text{Li}] = 0.25 \mu\text{g/L}$ ,  $\delta^7\text{Li} = +6\%$ , Fig. 5a). This suggests that for the Paleocene–Eocene boundary, riverine  $[\text{Li}]$  could have been significantly lower than it is today (Fig. 5a). However, it has to be appreciated that any mass balance calculation for past global Li cycles is affected by a relatively large uncertainty and it is beyond the scope of this study to provide accurate numbers for the one at the Paleocene–Eocene boundary. Without knowing the true global average riverine  $\delta^7\text{Li}$  and  $[\text{Li}]$  for the Paleocene–Eocene boundary, our study can thus not rule out a (minor) contribution from a changing seawater hydrothermal Li flux and a changing magnitude of oceanic Li isotopic fractionation on the Cenozoic seawater  $\delta^7\text{Li}$  increase.

## 5. Implications for using $\delta^7\text{Li}$ as a silicate weathering proxy

Previous studies did not show a distinct correlation between riverine  $\delta^7\text{Li}$  and traditional silicate weathering proxies such as  $[\text{Si}]$ , total cation charge  $\text{TZ}^+$  ( $\text{TZ}^+ = \text{Na}^+ + \text{K}^+ + 2\text{Mg}^{2+} + 2\text{Ca}^{2+}$ ), normalized  $[\text{Si}]$  ( $\text{Si}/\text{TZ}^+$ ),  $[\text{Li}]$ ,  $^{87}\text{Sr}/^{86}\text{Sr}$ , and  $\text{Li}/\text{Na}$  (Huh et al., 1998, 2001; Pogge von Strandmann et al., 2006; Millot et al., 2010; Pogge von Strandmann et al., 2010). For instance, Huh et al. (1998) did not observe a clear correlation between riverine  $\delta^7\text{Li}$  and  $^{87}\text{Sr}/^{86}\text{Sr}$ ,  $\delta^7\text{Li}$  and  $[\text{Li}]$ , as well as between  $\delta^7\text{Li}$  and  $\text{TZ}^+$ , whereas  $\delta^7\text{Li}$  tended to be slightly negatively correlated with  $\text{Si}/\text{TZ}^+$  when compiling available global river data. Completing the Huh et al. (1998) compilation with the numerous studies that have emerged since the original publication displays an even more random distribution between  $\delta^7\text{Li}$  and  $\text{TZ}^+$  (Fig. 7a). The same was observed for  $\delta^7\text{Li}$  vs.  $[\text{Li}]$  (Misra and Froelich, 2012). In contrast, the weak negative correlation between  $\delta^7\text{Li}$  and  $\text{Si}/\text{TZ}^+$  is still identified when updating the global river compilation (Fig. 7b). For specific river systems, additional correlations were observed. Examples include the strong inverse correlation between  $\delta^7\text{Li}$  and  $^{87}\text{Sr}/^{86}\text{Sr}$  as well as between  $\delta^7\text{Li}$  and  $\text{Si}/\text{TZ}^+$  observed for the Orinoco drainage basin (Huh et al., 2001) and the inverse correlation between  $\delta^7\text{Li}$  and  $[\text{Si}]$  as well as between  $\delta^7\text{Li}$  and  $[\text{Li}]$  observed in rivers draining mostly basalt (Pogge von Strandmann et al., 2010; 2006). More recently, Millot et al. (2010) and Liu et al. (in revision) have shown that  $\delta^7\text{Li}$  can display a negative correlation with  $\text{Li}/\text{Na}$  that also might have global significance. In fact, a negative correlation between  $\delta^7\text{Li}$  and  $\text{Li}/\text{Na}$  is also identified in our updated global river compilation (Fig. 7c).

Plotting  $[\text{Li}]$ ,  $[\text{Si}]$  and  $\text{TZ}^+$  along our model domain as well as against  $\delta^7\text{Li}$  reveals that  $\delta^7\text{Li}$  only forms a distinct correlation with such concentration proxies for a particular system (subsurface vs. river) (Figs. 4a–c and 5a–b). The transition from a positive correlation in the subsurface to a negative one within rivers occurs because once exfiltrated into a river, aqueous species concentrations decrease due to mixing with more diluted river water, while Li isotopic fractionation is ongoing. We thus propose that the identified great importance of Li isotopic fractionation occurring in rivers forms the main reason why concentration proxies do not show a distinct correlation with global riverine  $\delta^7\text{Li}$  values (e.g.,  $\delta^7\text{Li}$  vs.  $\text{TZ}^+$ , Fig. 7a;  $\delta^7\text{Li}$  vs.  $[\text{Li}]$ , Misra and Froelich, 2012). If Li isotopic fractionation was only occurring in the subsurface we would expect a positive correlation between  $\delta^7\text{Li}$  and concentrations proxies such as  $\text{TZ}^+$  (i.e., subsurface trend, Fig. 7a) because  $\delta^7\text{Li}$  and  $\text{TZ}^+$  (and any other concentration proxies) mainly reflect the subsurface residence time (Fig. 4a–b) as well as the corresponding weathering intensity (Fig. 5a–b). Instead, our simulations suggest that riverine  $\delta^7\text{Li}$  values reflect a particular combination of Li isotopic fractionation occurring within the subsurface as well as in rivers such as illustrated with the corresponding trends (Fig. 7a).

Subsurface and riverine trends shown in Fig. 7a are derived from simulating a monolithological subsurface that does not fully reach chemical equilibrium. Accordingly, the simulation results should be

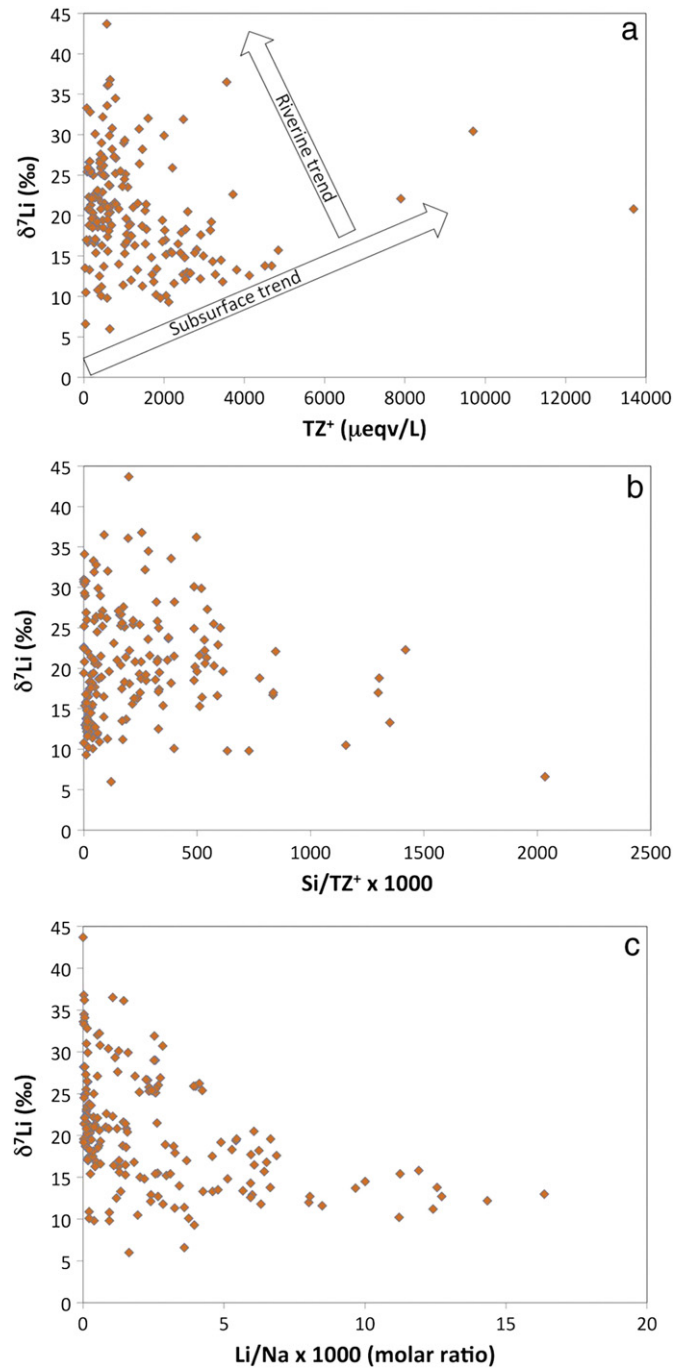


**Fig. 7.** Compilation of previously published riverine  $\delta^7\text{Li}$  (Huh et al., 1998, 2001; Pogge von Strandmann et al., 2006; Vigier et al., 2009; Millot et al., 2010; Pogge von Strandmann et al., 2010; Wimpenny et al., 2010b) plotted against various weathering tracers. (a)  $\delta^7\text{Li}$  vs.  $\text{TZ}^+$  ( $\text{TZ}^+ = [\text{Na}^+] + [\text{K}^+] + 2[\text{Ca}^{2+}] + 2[\text{Mg}^{2+}]$ ) and corresponding subsurface and riverine trend identified from simulation results (Fig. 4). (b)  $\delta^7\text{Li}$  vs.  $\text{Si}/\text{TZ}^+$ . (c)  $\delta^7\text{Li}$  vs.  $\text{Li}/\text{Na}$ . Samples affected by hydrothermal springs are not shown.

considered as simplified trends only. The observation that in natural aquifers  $\delta^7\text{Li}$  and  $[\text{Li}]$  are not always positively correlated (Tomascak et al., 2003; Négrel et al., 2010; Meredith et al., 2013) implies that additional parameters such as host rock mineralogy, hydrodynamic mixing of various groundwater types and aquifer residence time distribution in relation to chemical equilibrium (Maher, 2011) must be all taken into account to fully understand the relation between  $\delta^7\text{Li}$  and concentration proxies of a particular system (subsurface + river). Moreover,

we emphasize that the riverine trend in Fig. 7a does not imply that  $\delta^7\text{Li}$  is increasing with distance along a river, which would be in contradiction to field observations (Kisakürek et al., 2005; Pogge von Strandmann et al., 2006). For our river simulations a correlation between  $\delta^7\text{Li}$  and residence time (i.e., distance) is observed (Fig. 4a) because the ratio between Li isotopic fractionation occurring in rivers vs. the one occurring in aquifers is increasing with increasing river residence time. In other words, for natural rivers we only expect increasing riverine  $\delta^7\text{Li}$  with distance if the ratio of riverine Li isotopic fractionation vs. subsurface fractionation is increasing with flow distance. This ratio, however, is only changing if the subsurface residence time distribution is changing along a river.

Our simulation results agree well with the globally observed negative correlations between  $\delta^7\text{Li}$  and  $\text{Li}/\text{TZ}^+$  and between  $\delta^7\text{Li}$  and  $\text{Li}/\text{Na}$  (Fig. 7b–c) because the parameters that increase  $\delta^7\text{Li}$  (residence time increase, suspended river load concentration increase, weathering intensity decrease) cause a decrease in the simulated  $\text{Si}/\text{TZ}^+$  and  $\text{Li}/\text{Na}$  ratio (Figs. 4c and 5b). For a silicate setting also affected by newly formed secondary Ca- and Mg-bearing phases, we would expect a similar behavior for  $\text{Ca}/\text{TZ}^+$  and  $\text{Mg}/\text{TZ}^+$  as well as for  $\text{Ca}/\text{Na}$  and  $\text{Mg}/\text{Na}$ . The simulated negative correlation between  $\delta^7\text{Li}$  and  $\text{Si}/\text{TZ}^+$  as well as between  $\delta^7\text{Li}$  and  $\text{Li}/\text{Na}$  (Figs. 4c and 5b) is mainly observed because the  $\delta^7\text{Li}$  increase is inherited from an increasing amount of Li being incorporated in kaolinite and goethite with increasing aqueous [Li], whereas Na remains in solution. Precipitation of Li-bearing kaolinite also removes Si from the aqueous solution, which explains why  $\text{Si}/\text{TZ}^+$  is decreasing with increasing Si concentration (Figs. 4a–b and 5a). The  $\text{Si}/\text{TZ}^+$  decrease is most prominent if [Si] approaches a solubility controlled maximum such as observed towards the end of our subsurface domain (i.e.,  $t > 100\text{d}$ , Fig. 4a–b). In fact, the low sensitivity of  $\delta^7\text{Li}$  on  $\text{Si}/\text{TZ}^+$  for short subsurface residence times (Fig. 4b) is likely the reason why the negative correlation between  $\delta^7\text{Li}$  and  $\text{Si}/\text{TZ}^+$  is less pronounced than the one between  $\delta^7\text{Li}$  and  $\text{Li}/\text{Na}$  in global rivers (Fig. 7b–c).

### 5.1. Seawater $\delta^7\text{Li}$ : a proxy for Cenozoic continental silicate weathering rates?

We propose that  $\text{Si}/\text{TZ}^+$  as well as  $\text{Li}/\text{Na}$  are only particular and thus somewhat arbitrary proxies that correlate with  $\delta^7\text{Li}$  (Figs. 7b–c). Most importantly, it has not been shown yet how these ratios could serve as quantitative proxies for silicate weathering rates. We therefore postulate that the extent of water–rock interaction occurring along a particular flow path (subsurface + river) forms a more fundamental parameter that defines a system's  $\delta^7\text{Li}$ . In fact, our simulation results (Figs. 4c and 5b) clearly show that the amount of primary silicate mineral dissolution (quartz, feldspars, biotite) is positively correlated with  $\delta^7\text{Li}$ . The correlation occurs because the amount of mineral dissolution reflects an aquifer's residence time, the suspended river load concentration, and the weathering intensity, which have been identified to form the major controls on riverine  $\delta^7\text{Li}$ . Our simulations thus imply that aqueous  $\delta^7\text{Li}$  is highly correlated with the cumulative extent of water–rock interaction occurring along a particular flow path (in moles) suggesting that  $\delta^7\text{Li}$  is almost a perfect silicate weathering tracer. The positive correlation between  $\delta^7\text{Li}$  and silicate mineral dissolution (Figs. 4c and 5b), however, does not necessarily imply a correlation between  $\delta^7\text{Li}$  and silicate weathering rates (in mol/year). To obtain such weathering rates for a particular flow path, amounts of primary silicate mineral dissolution have to be multiplied by subsurface and riverine discharges. Subsurface and riverine discharges are closely related to the corresponding residence times. Accordingly, the previously identified lack of sensitivity of Cenozoic residence time variations on the Cenozoic seawater  $\delta^7\text{Li}$  record implies that this particular  $\delta^7\text{Li}$  record is not sensitive to discharge variations either. This finding is supported by Otto-Bliesner (1995) reporting that continental runoff remained roughly constant over the Cenozoic ( $\pm 10\%$ ).

Assuming minor effects from discharge variations, the simulated positive correlation between primary silicate mineral dissolution and riverine  $\delta^7\text{Li}$  (Figs. 4c and 5b) suggests that the Cenozoic seawater  $\delta^7\text{Li}$  increase (Misra and Froelich, 2012) was most likely caused by globally increasing continental silicate weathering rates. This finding strongly supports the Misra and Froelich (2012) hypothesis arguing that the Cenozoic seawater  $\delta^7\text{Li}$  increase is inherited from increasing riverine  $\delta^7\text{Li}$  values as a result of major Cenozoic tectonic uplift (e.g., Himalayan orogeny). The main argument for this statement is that uplift has a first order control on both parameters identified to increase silicate weathering rates as well as riverine  $\delta^7\text{Li}$  values (decreasing weathering intensity and increasing suspended river load concentration, Figs. 4c and 5a). This agreement is notable because our understanding of Li isotope fractionation processes does not rely on congruent weathering and is thus entirely different from the one of Misra and Froelich (2012).

In contrast to tectonic uplift, Cenozoic cooling occurring since the humid PETM (Miller et al., 1987; Clementz and Sewall, 2011) does not seem to have a distinct effect on  $\delta^7\text{Li}$ . Whereas Cenozoic cooling may have contributed to the Cenozoic weathering intensity decrease and corresponding  $\delta^7\text{Li}$  increase, cooling reduces the amount of primary silicate mineral dissolution along a specific flow path and drives  $\delta^7\text{Li}$  to lower values (Fig. 4c).  $\delta^7\text{Li}$  measurements from streams draining the Columbia River basalt under significantly different climatic conditions (dry vs. wet) confirm that climate does not necessarily have a first order control on riverine  $\delta^7\text{Li}$  (Liu et al., in revision).

## 6. Implications for $\text{CO}_2$ consumption by silicate weathering

The identified positive correlation between  $\delta^7\text{Li}$  and the amount of primary silicate mineral dissolution (Figs. 4c and 5b) suggests that, over the last 56 Ma, riverine  $\delta^7\text{Li}$  was closely correlated to the amount of  $\text{CO}_2$  consumed by silicate weathering reactions (Table 2) assuming that carbonic acid ( $\text{H}_2\text{O} + \text{CO}_2$ , Eq. (1)) forms the major proton source for these reactions and that continental discharge remained roughly constant (Otto-Bliesner, 1995). Accordingly, the Cenozoic seawater  $\delta^7\text{Li}$  record and the derived global average riverine  $\delta^7\text{Li}$  record provide a potential opportunity to quantify the amount of  $\text{CO}_2$  that was consumed by silicate weathering reactions throughout the Cenozoic.

In particular, reactive transport modeling such as performed here allows explicitly quantifying the amount of  $\text{CO}_2$  that was consumed along a specific flow path by integrating the amount of each mineral  $N_{\text{Mineral}}$  (mol) that was dissolved along the full model domain during a specific simulation period:

$$N_{\text{CO}_2} = 4 \cdot \sum N_{\text{albite}} + 8 \cdot \sum N_{\text{anorthite}} + 4 \cdot \sum N_{\text{Kspar}} + 10 \cdot \sum N_{\text{biotite}} + 0 \cdot \sum N_{\text{quartz}} - 6 \cdot \sum N_{\text{kaolinite}} - 2 \cdot \sum N_{\text{goethite}} \quad (11)$$

The dissolved mineral amounts ( $N_{\text{Mineral}}$ ) are scaled by the amount of  $\text{H}^+$  that is required to dissolve 1 mol of a specific mineral phases (e.g., 4 for albite, Table 2) because 1 mol of  $\text{H}^+$  is added to the solution (i.e.,  $\text{CO}_2$  is consumed by mineral dissolution) if 1 mol of atmospheric  $\text{CO}_2$  is dissolved (Eq. (1)). The amount of kaolinite precipitation times 6 and the amount of goethite precipitation times 2, respectively (i.e., stoichiometric coefficient of  $\text{H}^+$ , Table 2) were subtracted because kaolinite and goethite precipitation adds  $\text{H}^+$  to the system and liberates the same mole amount of  $\text{CO}_2$  to keep the  $p\text{CO}_2$  at the specified fixed value. It should be noted that Eq. (11) assumes that dissolved  $\text{HCO}_3^-$  precipitates as carbonates in the ocean (Fig. 1).

Applying Eq. (11) to our simulation runs indeed yields a positive correlation between  $\delta^7\text{Li}$  and  $\text{CO}_2$  consumption (Figs. 4c and 5b) implying that  $\text{CO}_2$  consumption by continental silicate weathering increased over the Cenozoic. This finding agrees well with the carbon cycle model of Li and Elderfield (2013) also suggesting an increase in continental silicate weathering and corresponding  $\text{CO}_2$  consumption rates over the Cenozoic. However, our modeling approach relies on

thermodynamic parameters for Li-bearing minerals that are only roughly constrained so far (e.g., fractionation factor, crystallographic substitution reaction, Li concentration of secondary minerals, Li solubility). Accordingly, our modeling approach should only be applied to qualitatively identify geochemical trends related to Li isotopic fractionation such as performed here. Once these thermodynamic parameters have been determined, a reliable quantification of the amount of CO<sub>2</sub> consumed by silicate weathering over the Cenozoic would require incorporating basalt weathering in addition to granite weathering, because basalt weathering accounts for more than 30% of global CO<sub>2</sub> consumption by silicate weathering even though basalts only form about 8% of exposed silicate rocks today (Gaillardet et al., 1999).

Our CO<sub>2</sub> consumption calculations also show that the amount of CO<sub>2</sub> consumed by pure “fresh granite” weathering (e.g., 100% contribution) was the same for the current and the Paleocene–Eocene weathering pattern simulations (17 kmol, Figs. 4b and 5b). The same applies for the simulated  $\delta^7\text{Li}$  values at the downstream subsurface model boundary (+10‰). This observation emphasizes that CO<sub>2</sub> consumption by continental silicate weathering reactions is more sensitive to specific primary silicate mineral phases that are exposed to chemical weathering rather than to atmospheric  $p\text{CO}_2$ . Moreover, it suggests that  $p\text{CO}_2$  variations during the Cenozoic (Li and Elderfield, 2013) do not seem to have a distinct control on the Cenozoic seawater  $\delta^7\text{Li}$  record.

To extend the use of seawater  $\delta^7\text{Li}$  values to reconstruct CO<sub>2</sub> consumption by continental silicate weathering for geological times other than the past 56 Ma, potential significant changes in continental river discharge have to be taken into account as well. Whereas discharge variations seem less important for the Cenozoic, a dramatic acceleration of the hydrological cycle caused by a short term atmospheric  $p\text{CO}_2$  increase shifted seawater  $\delta^7\text{Li}$  values by about –10‰ within a short period of time (100 ky) during Cretaceous Oceanic Anoxic Event 2 (OAE2) (Pogge von Strandmann et al., 2013). Because an accelerated hydrological cycle likely shifted discharge to higher values and residence times to lower values, the low OAE2  $\delta^7\text{Li}$  values correspond well with our simulated positive correlation between residence time and  $\delta^7\text{Li}$  (Fig. 4a). Interestingly, the negative  $\delta^7\text{Li}$  excursion observed for OAE2 was attributed to enhanced continental silicate weathering forming a negative feedback on the inferred  $p\text{CO}_2$  increase (Pogge von Strandmann et al., 2013). This finding is opposite to the one made for the Cenozoic because for the past 56 Ma, inferred increasing silicate weathering rates are manifested by a  $\delta^7\text{Li}$  increase (Misra and Froelich, 2012; this study) while for OAE2 they are accompanied by a  $\delta^7\text{Li}$  decrease (Pogge von Strandmann et al., 2013). This apparent contradiction is, however, well explained by our modeling results revealing that seawater and inferred riverine  $\delta^7\text{Li}$  values are simply a function of the amount of silicate weathering and corresponding CO<sub>2</sub> consumption along a specific flow path (in moles) (Figs. 4c and 5b). However, they are not necessarily correlated with silicate weathering and CO<sub>2</sub> consumption rates (in mol/year) on which discharge has a first order control (Gaillardet et al., 1999). The opposing behavior of  $\delta^7\text{Li}$  with increasing silicate weathering rates thus highlights the importance of reconstructing past discharge rates, which, owing to the strong correlation between silicate weathering rates and discharge (Gaillardet et al., 1999), is indispensable for quantifying past CO<sub>2</sub> consumption rates based on seawater  $\delta^7\text{Li}$  measurements.

## 7. Summary and conclusions

A novel reactive transport modeling approach was developed to simulate Li isotopic fractionation during Li uptake by secondary mineral phases. Simulation results show that riverine  $\delta^7\text{Li}$  is controlled not only by the Li isotopic fractionation factor but also by the subsurface residence time of infiltrating meteoric water, the corresponding weathering intensity and the concentration of a river's suspended load.

Based on these identified factors, we presented a new interpretation of the previously reported Cenozoic seawater  $\delta^7\text{Li}$  record (Misra and

Froelich, 2012) that does not rely on geochemically unlikely congruent weathering. In particular, modeling results imply that the low seawater  $\delta^7\text{Li}$  observed at the Paleocene–Eocene boundary could be inherited from a high weathering intensity with predominant weathering of previously-formed secondary mineral phases (e.g., clays, oxides, hydroxides) having a low  $\delta^7\text{Li}$  and a low contribution of incongruent silicate mineral dissolution with associated secondary mineral formation and Li isotopic fractionation. Moreover, simulation results imply that the Cenozoic seawater  $\delta^7\text{Li}$  increase was likely caused by an increasing amount of primary silicate mineral dissolution (i.e., decreasing weathering intensity, increasing suspended river load concentration) inherited from tectonic uplift and a corresponding global relief increase. In contrast, Cenozoic cooling and corresponding  $p\text{CO}_2$  and precipitation variations do not seem to have a distinct control on the Cenozoic seawater  $\delta^7\text{Li}$  record. It is thus emphasized that our modeling results strongly favor the original Raymo and Ruddiman (1992) model stating that a tectonically-driven increase in silicate weathering rates may have caused the inferred Cenozoic atmospheric  $p\text{CO}_2$  decrease. However, another Li isotope study has shown that for dramatic, short term events increasing atmospheric  $p\text{CO}_2$  and triggering warmer temperatures (e.g., Cretaceous OAE2), silicate weathering and corresponding CO<sub>2</sub> consumption rates can be dramatically increased without major tectonic uplift (Pogge von Strandmann et al., 2013).

The identified strong correlation between Cenozoic silicate weathering rates and  $\delta^7\text{Li}$  implies that seawater and global average riverine  $\delta^7\text{Li}$  values are closely related to global CO<sub>2</sub> consumption by continental silicate weathering. For an actual quantitative correlation, however, more experimental and modeling work is required. Key parameters are the temperature-dependent thermodynamic properties of specific Li bearing primary and secondary minerals (e.g., crystallographic Li substitution and surface complexation reactions, maximum Li substitution, Li solubility, Li isotopic fractionation factor) as well as the determination of global average continental discharge through time.

Incorporating Li isotopic fractionation into reactive transport model simulations of subsurface and river systems also improved the understanding of the  $\delta^7\text{Li}$  distribution observed in global rivers today. Simulation results revealed that Li isotopic fractionation occurs in the subsurface as well as in river systems. Fractionation occurring in both systems seems to be the main reason why no or only weak correlations between global riverine  $\delta^7\text{Li}$  values and traditional silicate weathering proxies such as [Si], [Li], Si/TZ<sup>+</sup> are observed. The lack of correlation is observed because once exfiltrated into rivers, elemental concentrations are diluted by a larger flux of superficial river waters while Li isotopic fractionation is still ongoing.

Finally, this study illustrates that reactive transport modeling is a powerful tool for a (semi)-quantitative interpretation of stable isotope ratios. In comparison to closed system Rayleigh-type or steady state flux models, it bears the advantage of considering the full thermodynamic properties of involved mineral phases (e.g., mineral stoichiometry, mineral solubility, kinetic dissolution/precipitation) as well as assessing the effect of transport on isotopic fractionation. The presented solid solution approach can be easily applied to other isotopic systems (e.g., Si, Mg, Ca, Mo), which have also been shown to serve as potentially powerful weathering proxies (Ziegler et al., 2005; Tipper et al., 2012; Voegelin et al., 2012; Moore et al., 2013).

## Acknowledgments

This work was supported by the U.S. Department of Energy, Geothermal Technologies Program, Energy Efficiency and Renewable Energy Office, award no. GT-480010-12. Postdoctoral fellowship support was provided to X-ML by the Carnegie Institution of Washington. The manuscript significantly benefited from a helpful editorial handling by Michael Böttcher, and very constructive comments by Philip Pogge von Strandmann and an additional, anonymous reviewer.

## References

- Berner, R.A., 1994. 3GEOCARB II: a revised model of atmospheric CO<sub>2</sub> over Phanerozoic time. *Am. J. Sci.* 294, 56–91.
- Berner, R.A., Kothavala, Z., 2001. GEOCARB III: a revised model of atmospheric CO<sub>2</sub> over Phanerozoic time. *Am. J. Sci.* 301, 182–204.
- Berner, R.A., Lasaga, A.C., Garrels, R.M., 1983. The carbonate-silicate geochemical cycle and its effect on atmospheric carbon-dioxide over the past 100 million years. *Am. J. Sci.* 283, 641–683.
- Bouchez, J., Gaillardet, J., France-Lanord, C., Maurice, L., Dutra-Maia, P., 2011. Grain size control of river suspended sediment geochemistry: clues from Amazon River depth profiles. *Geochem. Geophys. Geosyst.* 12, Q03008.
- Bouchez, J., Von Blanckenburg, F., Schuessler, J.A., 2013. Modeling novel stable isotope ratios in the weathering zone. *Am. J. Sci.* 313, 267–308.
- Clementz, M.T., Sewall, J.O., 2011. Latitudinal gradients in greenhouse seawater δ<sup>18</sup>O: evidence from Eocene Sirenian Tooth Enamel. *Science* 332, 455–458.
- Decarreau, A., Vigier, N., Pálková, H., Petit, S., Vieillard, P., Fontaine, C., 2012. Partitioning of lithium between smectite and solution: an experimental approach. *Geochim. Cosmochim. Acta* 85, 314–325.
- Dobson, P.F., Kneafsey, T.J., Sonnenthal, E.L., Spycher, N., Apps, J.A., 2003. Experimental and numerical simulation of dissolution and precipitation: implications for fracture sealing at Yucca Mountain, Nevada. *J. Cotam. Hydrol.* 62–63, 459–476.
- Du Laing, G., Rinklebe, J., Vandecasteele, B., Meers, E., Tack, F.M.G., 2009. Trace metal behaviour in estuarine and riverine floodplain soils and sediments: a review. *Sci. Total Environ.* 407, 3972–3985.
- Economos, R.C., Memeti, V., Paterson, S.R., Miller, J.S., Erdmann, S., Zak, J., 2010. Causes of compositional diversity in a lobe of the Half Dome granodiorite, Tuolumne Batholith, Central Sierra Nevada, California. *Earth Environ. Sci. Trans. R. Soc.* 100, 173–183.
- Edmond, J.M., Palmer, M.R., Measures, C.I., Grant, B., Stallard, R.F., 1995. The fluvial geochemistry and denudation rate of the Guayana Shield in Venezuela, Colombia, and Brazil. *Geochim. Cosmochim. Acta* 59, 3301–3325.
- Francois, L.M., Godderis, Y., 1998. Isotopic constraints on the Cenozoic evolution of the carbon cycle. *Chem. Geol.* 145, 177–212.
- Fryirs, K.A., Brierley, G.J., 2013. *Geomorphologic Analysis of River Systems: An Approach to Reading the Landscape*. John Wiley & Sons.
- Gaillardet, J., Dupré, B., Louvat, P., Allègre, C.J., 1999. Global silicate weathering and CO<sub>2</sub> consumption rates deduced from the chemistry of large rivers. *Chem. Geol.* 159, 3–30.
- Godderis, Y., Roelandt, C., Schott, J., Pierret, M., Francois, L.M., 2009. Towards an integrated model of weathering, climate, and biosphere processes. In: Oelkers, E.H., Schott, J. (Eds.), *Towards an integrated model of weathering, climate, and biosphere processes*. Mineralogical Society of America. *Rev. Mineral.* 70, pp. 411–434.
- Hathorne, E.C., James, R.H., 2006. Temporal record of lithium in seawater: a tracer for silicate weathering. *Earth Planet. Sci. Lett.* 246, 393–406.
- Huh, Y., Chan, L.H., Zhang, L., Edmond, J.M., 1998. Lithium and its isotopes in major world rivers: implications for weathering and the oceanic budget. *Geochim. Cosmochim. Acta* 62, 2039–2051.
- Huh, Y., Chan, L.H., Edmond, J.M., 2001. Lithium isotopes as a probe of weathering processes: Orinoco River. *Earth Planet. Sci. Lett.* 194, 189–199.
- Huh, Y., Chan, L.H., Chadwick, O.A., 2004. Behavior of lithium and its isotopes during weathering of Hawaiian basalt. *Geochem. Geophys. Geosyst.* 5, Q09002.
- Johnson, J.W., Oelkers, E.H., Helgeson, H.C., 1992. SUPCRT92: a software package for calculating the standard molal thermodynamic properties of minerals, gases, aqueous species, and reactions from 1 to 5000 bar and 0 to 1000 °C. *Comput. Geosci.* 18, 899–948.
- Keeling, C.D., 1960. The concentration and isotopic abundances of carbon dioxide in the atmosphere. *Tellus* 12, 200–203.
- Kisakürek, B., Widdowson, M., James, R.H., 2004. Behaviour of Li isotopes during continental weathering: the Bidar laterite profile, India. *Chem. Geol.* 212, 27–44.
- Kisakürek, B., James, R.H., Harris, N.B.W., 2005. Li and δ<sup>7</sup>Li in Himalayan rivers: proxies for silicate weathering? *Earth Planet. Sci. Lett.* 237, 387–401.
- Kretz, R., Loop, J., Hartree, R., 1989. Petrology and Li–Be–B geochemistry of muscovite-biotite granite and associated pegmatite near Yellowknife, Canada. *Contrib. Mineral. Petrol.* 102, 174–190.
- Lasaga, A.C., 1984. Chemical kinetics of water–rock interactions. *J. Geophys. Res.* 89, 4009–4025.
- Lemarchand, E., Chabaux, F., Vigier, N., Millot, R., Pierret, M.-C., 2010. Lithium isotope systematics in a forested granitic catchment (Strengbach, Vosges Mountains, France). *Geochim. Cosmochim. Acta* 74, 4612–4628.
- Li, G., Elderfield, H., 2013. Evolution of carbon cycle over the past 100 million years. *Geochim. Cosmochim. Acta* 103, 11–25.
- Li, G., West, A.J., 2014. Increased continental weathering flux through the Cenozoic inferred from the lithium isotope evolution of seawater. *Earth Planet. Sci. Lett.* (accepted for publication).
- Liu, X.-M., Rudnick, R.L., McDonough, W.F., Cummings, M.L., 2013. Influence of chemical weathering on the composition of the continental crust: insights from Li and Nd isotopes in bauxite profiles developed on Columbia River Basalts. *Geochim. Cosmochim. Acta* 115, 73–91.
- Liu, X.-M., Wanner, C., Rudnick, R.L., McDonough, W.F., 2014. Novel interpretation of large Li isotopic variations produced by streams and ground waters draining basalts. *Earth Planet. Sci. Lett.* (in revision).
- Maher, K., 2011. The role of fluid residence time and topographic scales in determining chemical fluxes from landscapes. *Earth Planet. Sci. Lett.* 312, 48–58.
- Maher, K., Steefel, C.I., White, A.F., Stonestrom, D.A., 2009. The role of reaction affinity and secondary minerals in regulating chemical weathering rates at the Santa Cruz Soil Chronosequence, California. *Geochim. Cosmochim. Acta* 73, 2804–2831.
- Meredith, K., Moriguti, T., Tomascak, P., Hollins, S., Nakamura, E., 2013. The lithium, boron and strontium isotopic systematics of groundwaters from an arid aquifer system: implications for recharge and weathering processes. *Geochim. Cosmochim. Acta* 112, 20–31.
- Miller, K.G., Fairbanks, R.G., Mountain, G.S., 1987. Tertiary oxygen isotope synthesis, sea level history, and continental margin erosion. *Paleoceanography* 2, 1–19.
- Milliman, J.D., Meade, R.H., 1983. World-wide delivery of river sediment to the oceans. *J. Geol.* 91, 1–21.
- Millot, R., Vigier, N., Gaillardet, J., 2010. Behaviour of lithium and its isotopes during weathering in the Mackenzie Basin, Canada. *Geochim. Cosmochim. Acta* 74, 3897–3912.
- Misra, S., Froelich, P.N., 2012. Lithium isotope history of Cenozoic seawater: changes in silicate weathering and reverse weathering. *Science* 335, 818–823.
- Moore, J., Jacobson, A.D., Holmden, C., Craw, D., 2013. Tracking the relationship between mountain uplift, silicate weathering, and long-term CO<sub>2</sub> consumption with Ca isotopes: Southern Alps, New Zealand. *Chem. Geol.* 341, 110–127.
- Müller, R.D., Sdrolias, M., Gaina, C., Steinberger, B., Heine, C., 2008. Long-term sea-level fluctuations driven by ocean basin dynamics. *Science* 319, 1357–1362.
- Négrel, P., Millot, R., Brenot, A., Bertin, C., 2010. Lithium isotopes as tracers of groundwater circulation in a peat land. *Chem. Geol.* 276, 119–127.
- Nesbitt, H.W., Young, G.M., 1982. Early Proterozoic climates and plate motions inferred from major element chemistry of lutes. *Nature* 299, 715–717.
- Oliver, L., Harris, N., Bickle, M., Chapman, H., Dise, N., Horstwood, M., 2003. Silicate weathering rates decoupled from the <sup>87</sup>Sr/<sup>86</sup>Sr ratio of the dissolved load during Himalayan erosion. *Chem. Geol.* 201, 119–139.
- Otto-Bliesner, B.L., 1995. Continental drift, runoff, and weathering feedbacks: implications from climate model experiments. *J. Geophys. Res.-Atmos.* 100, 11537–11548.
- Palandri, J.L., Kharaka, Y.K., 2004. A compilation of rate parameters of water–mineral interaction kinetics for application to geochemical modeling. *US Geological Survey. Report* 2004-1068.
- Pistiner, J.S., Henderson, G.M., 2003. Lithium-isotope fractionation during continental weathering processes. *Earth Planet. Sci. Lett.* 214, 327–339.
- Pogge von Strandmann, P.A.E., Burton, K.W., James, R.H., van Calsteren, P., Gislason, S.R., Mokadem, F., 2006. Riverine behaviour of uranium and lithium isotopes in an actively glaciated basaltic terrain. *Earth Planet. Sci. Lett.* 251, 134–147.
- Pogge von Strandmann, P.A.E., Burton, K.W., James, R.H., van Calsteren, P., Gislason, S.R., 2010. Assessing the role of climate on uranium and lithium isotope behaviour in rivers draining a basaltic terrain. *Chem. Geol.* 270, 227–239.
- Pogge von Strandmann, P.A.E., Jenkyns, H.C., Woodfine, R.G., 2013. Lithium isotope evidence for enhanced weathering during Oceanic Anoxic Event 2. *Nat. Geosci.* 6, 668–672.
- Raymo, M.E., Ruddiman, W.F., 1992. Tectonic forcing of late Cenozoic climate. *Nature* 359, 117–122.
- Reed, M., Palandri, J.L., 2006. *SOLTherm.H06, A Database of Equilibrium Constants for Minerals and Aqueous Species*. Available from the Authors. University of Oregon, Eugene.
- Rowley, D.B., 2002. Rate of plate creation and destruction: 180 Ma to present. *Geol. Soc. Am. Bull.* 114, 927–933.
- Rudnick, R.L., Tomascak, P.B., Njo, H.B., Gardner, L.R., 2004. Extreme lithium isotopic fractionation during continental weathering revealed in saprolites from South Carolina. *Chem. Geol.* 212, 45–57.
- Singleton, M.J., Sonnenthal, E.L., Conrad, M.E., DePaolo, D.J., Gee, G.W., 2005. Multiphase reactive transport modeling of seasonal infiltration events and stable isotope fractionation in unsaturated zone pore water and vapor at the Hanford site. *Vadose Zone J.* 3, 775–785.
- Sonnenthal, E.L., Spycher, N., Apps, J.A., Simmons, A., 1998. *Thermo-hydro-chemical Predictive Analysis for the Drift-scale Heater Test*. Lawrence Berkeley National Laboratory (Level 4 Milestone SPY289M4).
- Steeffel, C.I., DePaolo, D.J., Lichtner, P.C., 2005. Reactive transport modeling: an essential tool and a new research approach for the Earth sciences. *Earth Planet. Sci. Lett.* 240, 539–558.
- Tardy, Y., Nahon, D., 1985. Geochemistry of laterites, stability of Al-goethite, Al-hematite, and Fe<sup>3+</sup>-kaolinite in bauxites and ferricretes – an approach to the mechanism of concretion formation. *Am. J. Sci.* 285, 865–903.
- Tardy, Y., Trauth, N., Krempff, G., 1972. Lithium in clay-minerals of sediments and soils. *Geochim. Cosmochim. Acta* 36, 397.
- Teng, F.Z., McDonough, W.F., Rudnick, R.L., Dalpé, C., Tomascak, P.B., Chappell, B.W., Gao, S., 2004. Lithium isotopic composition and concentration of the upper continental crust. *Geochim. Cosmochim. Acta* 68, 4167–4178.
- Teng, F.-Z., Rudnick, R.L., McDonough, W.F., Gao, S., Tomascak, P.B., Liu, Y., 2008. Lithium isotopic composition and concentration of the deep continental crust. *Chem. Geol.* 255, 47–59.
- Teng, F.-Z., Rudnick, R.L., McDonough, W.F., Wu, F.-Y., 2009. Lithium isotopic systematics of A-type granites and their mafic enclaves: further constraints on the Li isotopic composition of the continental crust. *Chem. Geol.* 262, 370–379.
- Tipper, E.T., Calmels, D., Gaillardet, J., Louvat, P., Capmas, F., Dubacq, B., 2012. Positive correlation between Li and Mg isotope ratios in the river waters of the Mackenzie Basin challenges the interpretation of apparent isotopic fractionation during weathering. *Earth Planet. Sci. Lett.* 333–334, 35–45.
- Tomascak, P.B., Hemming, N.G., Hemming, S.R., 2003. The lithium isotopic composition of waters of the Mono Basin, California. *Geochim. Cosmochim. Acta* 67, 601–611.
- Vigier, N., Decarreau, A., Millot, R., Carignan, J., Petit, S., France-Lanord, C., 2008. Quantifying Li isotope fractionation during smectite formation and implications for the Li cycle. *Geochim. Cosmochim. Acta* 72, 780–792.
- Vigier, N., Gislason, S.R., Burton, K.W., Millot, R., Mokadem, F., 2009. The relationship between riverine lithium isotope composition and silicate weathering rates in Iceland. *Earth Planet. Sci. Lett.* 287, 434–441.

- Voegelin, A.R., Nägler, T.F., Pettke, T., Neubert, N., Steinmann, M., Pourret, O., Villa, I.M., 2012. The impact of igneous bedrock weathering on the Mo isotopic composition of stream waters: natural samples and laboratory experiments. *Geochim. Cosmochim. Acta* 86, 150–165.
- Wanner, C., Sonnenthal, E.L., 2013. Assessing the control on the effective kinetic Cr isotope fractionation factor: a reactive transport modeling approach. *Chem. Geol.* 337, 88–98.
- White, A.F., 2002. Determining mineral weathering rates based on solid and solute weathering gradients and velocities: application to biotite weathering in saprolites. *Chem. Geol.* 190, 69–89.
- White, A.F., Bullen, T.D., Schulz, M.S., Blum, A.E., Huntington, T.G., Peters, N.E., 2001. Differential rates of feldspar weathering in granitic regoliths. *Geochim. Cosmochim. Acta* 65, 847–869.
- Wimpenny, J., Gislason, S.R., James, R.H., Gannoun, A., Pogge Von Strandmann, P.A.E., Burton, K.W., 2010a. The behaviour of Li and Mg isotopes during primary phase dissolution and secondary mineral formation in basalt. *Geochim. Cosmochim. Acta* 74, 5259–5279.
- Wimpenny, J., James, R.H., Burton, K.W., Gannoun, A., Mokadem, F., Gislason, S.R., 2010b. Glacial effects on weathering processes: new insights from the elemental and lithium isotopic composition of West Greenland rivers. *Earth Planet. Sci. Lett.* 290, 427–437.
- Wimpenny, J., Colla, C.A., Yin, Q.-Z., Rustad, J.R., Casey, W.H., 2014. Investigating the behaviour of Mg isotopes during the formation of clay minerals. *Geochim. Cosmochim. Acta* 128, 178–194.
- Xu, T., Spycher, N., Sonnenthal, E.L., Zhang, G., Zheng, L., Pruess, K., 2011. TOUGHREACT Version 2.0: a simulator for subsurface reactive transport under non-isothermal multiphase flow conditions. *Comput. Geosci.* 37, 763–774.
- Yang, L., Steefel, C.I., 2008. Kaolinite dissolution and precipitation kinetics at 22 °C and pH 4. *Geochim. Cosmochim. Acta* 72, 99–116.
- Yoon, J., 2010. Lithium as a silicate weathering proxy: problems and perspectives. *Aquat. Geochem.* 16, 189–206.
- Zhang, L., Chan, L.-H., Gieskes, J.M., 1998. Lithium isotope geochemistry of pore waters from ocean drilling program Sites 918 and 919, Irminger Basin. *Geochim. Cosmochim. Acta* 62, 2437–2450.
- Ziegler, K., Chadwick, O.A., Brzezinski, M.A., Kelly, E.F., 2005. Natural variations of  $\delta^{30}\text{Si}$  ratios during progressive basalt weathering, Hawaiian Islands. *Geochim. Cosmochim. Acta* 69, 4597–4610.